Università degli Studi di Padova

Dipartimento di Fisica e Astronomia "Galileo Galilei"

Corso di Laurea Magistrale in Astrophysics & Cosmology

Pontus and Gaia-Sausage/Enceladus: insights from the orbital properties of candidates members

Relatore

Prof. Giovanni Carraro

Laureando

Andrea Cichellero

Matricola: 2016969

Anno Accademico 2021/2022

If I were a hummingbird
Your wings would beat like thunder
Orbit in a flight display
As if to gently say
Kiss the flowers ultraviolet
We could get lost or we could find it alive with
Electrons in the air on fire
Lightning kissing metal
Whisper to the tiny hairs
Battery on my tongue
Meteor that greets Sahara
We could get lost in static power

"Chivalry Is Not Dead"
Nai Palm, Hiatus Kaiyote

Abstract

Merging events between progenitor galaxies represent the baseline of the origin of the Milky Way halo, and an important role is described by the globular clusters that originated during these events. Taking into account different potential models, the current work describes the globular cluster population associated with two major merging events: Gaia-Sausage/Enceladus and Pontus, a newly discovered merger. The WHVN algorithm was developed to integrate orbits, starting from Gaia EDR3 data, and to calculate different orbital parameters, such as angular momentum, total energy, and eccentricity, of the entire globular cluster population, with particular attention to Gaia-Sausage/Enceladus and Pontus candidates. Results show that all major candidates for both events are confirmed and separated, with error propagation performed using Monte Carlo and Gauss scattering methods. Eventually, deeper and more characterised studies will shed additional insights on merging events, especially on the newest Pontus merger.

Contents

Chapter 1

Origin of galaxy and merging events

All of the Galaxy's structural components play a significant role in Galactic evolution as well as their own evolutionary history, and their stellar populations may give more insights into the early stages of the Milky Way.

In particular, the following work highlights how the so-called merging events can properly describe the origin of the Milky Way's dark matter halo; the process through which larger structures are built by the ongoing merging of smaller ones is known as hierarchical clustering, and according to cold dark matter (CDM) cosmology, the structures observed in the Universe today are believed to have developed according to this process. The current study is focused on the dynamical properties obtained by modelling the various components of the Milky Way (bulge, bar, disk, and halo), while keeping an eye open to its progenitors.

Most galaxies undergo changes on a wide range of spatial and temporal scales, and the degree to which this evolution contributes to various Galactic components has always been a topic of interest in Galactic dynamics. As described in [Gilmore & Feltzing, 1999], different approaches via numerical models supported the creation and disintegration of spiral structures and bars, alongside bulge formation from discs.
Previous studies contained in [Gilmore, 1996] work found that a specific correlation between stellar orbital eccentricity and metallicity implies a rapid collapse of the early halo into the disk, based on the assumption that all the gas that is today in the Milky Way's potential well has always been there, but dark matter-dominated models for galaxy formation initially denied this assumption.
More in-depth photometric measurements were acceptable but needed a better explanation. That was provided later thanks to the bulge's rotation curves and distributions of angular momentum of the various Galactic structural components; these latter distributions were seen in both the thick and old disk as well as the metal-poor halo and bulge; so the correlation represented evidence of an early monolithic collapse of the halo into the bulge (not the disc as assumed previously).
Moreover, another interesting open topic in [Gilmore, 1996] paper was the presence of the Sagittarius Dwarf Spheroidal Galaxy (Sgr dSph) well inside the Milky Way. Its existence represented one of the main reasons for proceeding with deeper studies on later mergers associated with the contents of the early halo. The robust character of Sgr dSph against tidal distruption supported the cold dark matter dominance inside dwarf spheroidals, which was confirmed with subsequent numerical calculations. At the time, a lot of data for the age distribution of halo stars was available, together with discoveries regarding the dark matter-dominated dwarf spheroidals; finally, it was clear that the present halo and

the outer bulge are dominated by early stellar populations formed in the potential well. The discovery supported the idea of the relationship between mergers and halo origin, and it opened subsequent studies on different mergers that will be discussed in detail in the next sections.

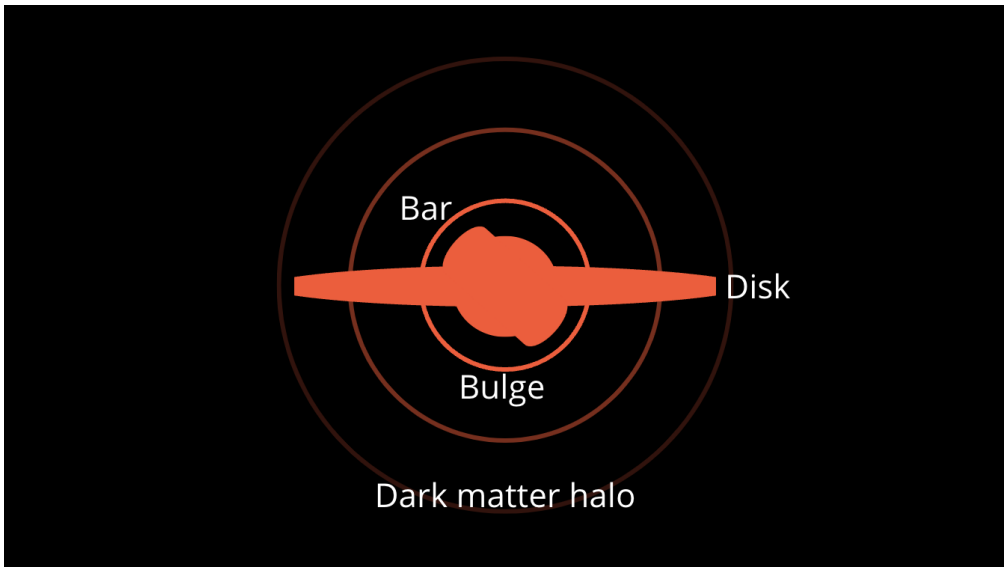

Figure 1.1: Milky Way scheme. Credits: Andrea Cichellero.

In addition, a phenomenological study was conducted by [White & Frenk, 1991], developing analytic methods for studying the formation of galaxies by gas condensation inside massive dark halos, which were applied to systems where hierarchical clustering of a mixture of gas and dissipationless dark matter took place.
Different models for the evolution of stellar populations were based on the way star formation heats and enriches the surrounding gas, therefore it was possible to predict star formation as a function of location and time, plus different features of the Milky Way's population. These predictions had a strong dependency on the mean baryon density, on the models for heating and metal enrichment from massive stars, and on the initial mass function with which stars form. Results showed that additional sources were needed because the obtained luminosity functions contained more faint galaxies than the observed ones. This issue supported the theory of the merging of dwarf galaxies with observational support from a selection of low surface brightness dwarf galaxies.

Another approach was presented by [Lacey & Cole, 1993] based on the merging of dark matter halos with a hierarchical model where the growth is set by a gravitational instability. The merger rate is primarily determined by the mass of the halo, epoch, and spectrum of initial density fluctuations; results suggest that a high density parameter (Ω_0) is required to sustain overserved clusters. Another important result consists of the low infall rate of satellite galaxies into the Galactic disk, where early assumptions give a small fraction of stellar discs thickened or destroyed by the merger.

Present star clusters could also be explained from the collision and merging of small gas-rich subclusters originated by the collapse of giant molecular clouds, according to the most recent work by [Karam & Sills, 2022]: authors provided simulations in which these subclusters collide according to N-body dynamics for star population and hydrodynamic models for gas particles.
Different tests gave an upper limit for the final cluster. Simulations driven by the colliding subclusters do not return monolithic clusters within 3 Myr, but eventually they could merge on timescales longer than the time for the next collision.

Overall, the origin of dark matter haloes based on merging events of dwarf galaxies and connected to present star clusters is strongly supported in literature, and yet deeper studies have to be done whenever a new event is discovered.
Furthermore, star clusters can provide crucial informations about the origin of the Milky Way via their orbits around the Galactic Centre, as they are strongly connected to the physical features and intrinsic origin of the Galaxy, according to [Malhan et al. 2022] and [Naidu et al. 2020]. One can determine the orbits of a star cluster from the initial position and velocities in the phase-space, but first a legitimate description of the system must be made, considering all the contributors to the potential equilibrium.

In the current context, a new algorithm called WHVN ("What History Vanishes Now") was developed by the author of this thesis based on the GALA and AstroPy packages and used to solve the equations of motion for specific targets using two custom gravitational potential models with Gaia EDR3–based measurements of 170 globular clusters. Under these hypotheses, the angular momentum, energy of the system, and other orbital parameters can be calculated to provide crucial information about the cluster's origin in a merging event.

Section 1.1 will provide a general description of each Milky Way component, while section 1.2 will provide information on various merging events, particularly two major mergers, Gaia-Sausage/Enceladus and Pontus.

1.1 Galaxy structure

Giving the spiral nature of the Milky Way, three main components can be described: disk, halo, and bulge, where the latter can show the rotating bar feature. Usually, bulge stars tend to be old and metal poor, while younger stars can be found in the disk with a huge amount of gas and dust that are quite absent in bulges; in particular, bulges are the hottest components in which random motions dominate. Overall, observational rotation curves of spiral galaxies have two main features: one solid body increase in the central regions, with a subsequent flat section where the velocity as a function of the distance is constant. The presence of the dark matter halo causes the flattening of the rotation curves.

Disk

Most stars in the Galaxy, according to simple observations on a clear night, lie on a disk as a flat and quite axisymmetric structure, resembling a massive group of faint stars arranged as a luminous band in the night sky.

Following [Binney & Tremaine, 2008] outline, the Galactic plane is defined as the midplane of the disk, where it is possible to set the Galactic coordinates (l, b), respectively, the Galactic longitude and the Galactic latitude. The origin of this coordinate system is based on the Galactic center's position with respect to the Sun's position (due to the heliocentric nature of the coordinate system): in this spherical framework, the Galactic centre has coordinates $(l, b) = (0, 0)$, while the Galactic poles are positioned at $b = \pm 90°$.

The distance of the Sun from the Galactic Center is denoted as $R_\odot$, usually estimated at $R_\odot = (8.0 \pm 0.5)$ kpc. Also, measuring the scale length of the disk is challenging due to the Sun's position within the disk; according to [Binney & Tremaine, 2008], about 75–90% of the disk stars are closer to the Galactic centre than the Sun is, and so there is a high luminosity covered by dust towards $(l, b) = (0, 0)$. In the infrared regime, dust

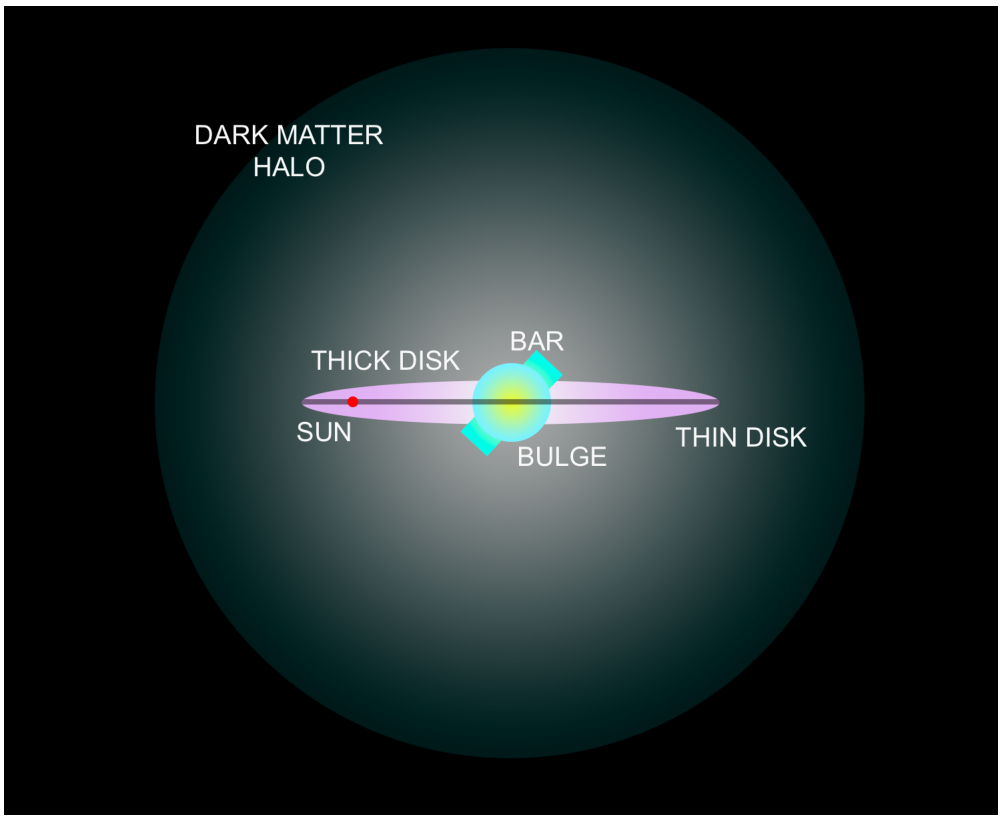

Figure 1.2: Milky Way components and the Sun's position. Credits: Andrea Cichellero.

extinction is negligible, so a huge light concentration can be seen near the constellation of Sagittarius; in contrast, towards the galactic poles, the Milky Way appears transparent.

Disk stars have a characteristic nearly-circular orbit around the Galactic centre, but measurements of their motion are strongly influenced by the SgrA* radio source. While the density of stars decreases exponentially in the perpendicular direction of the Galactic plane, some information can be obtained by measuring the disk thickness; in particular, older stellar populations ($\sim$10 Gyr) have a larger scale height, while it decreases for young O and B stars.

Moreover, the disk region can be divided into two main sections: the thick disk and the thin disk. In particular, the thick disk, with a thickness of around 1 kpc, shows lower metallicity than the thin disk, and at fixed metallicity, the $[\alpha/H]$ abundance is higher than the thin disk; the latter feature is actually a consequence of the gas that was processed in the early galaxy phases by Core Collapse Supernovae and Type Ia Supernovae. Typically, a thick disk is characterised by a lower surface density of stars and a lower number density, probably because the thick disk originated from a young thin disk.

Dark matter halo

Dark matter haloes are described as hypothetical regions formed by gravitationally bound matter with which cosmological models (such as ΛCDM) associate the presence of galaxies. They are usually extended halos with corresponding subhalos, smaller clumps of dark matter that are in virial equilibrium with gravity. Haloes are bigger than the disk extension, and their radius is higher than the radius of the visible galaxy. As many cosmological studies have confirmed over the past 25 years, Milky Way formation and evolution are supported by dark matter halos.

In the first [Navarro et al. 1996] work, N-body simulations attempted to shed light on the structure of dark haloes in the cold dark matter theory, studying various halo mass ranges, from dwarf galaxy halos to rich galaxy clusters.

The halo concentration (or the halo over-density) correlates strongly with its mass, giving information about the epoch of its formation. Halos are usually seen as isothermal within huge radii, but they change depending on the radius dependence in the density profile used.
In bright galaxies, the halo depends poorly on Galactic luminosity, showing lower circular velocities than disk rotation speed, and this can be seen by comparing observed rotation curves of disk galaxies with required mass-to-light ratios. This important result gives an answer to the absent correlation between the luminosity and dynamics of binary galaxies and of satellite/spiral systems.

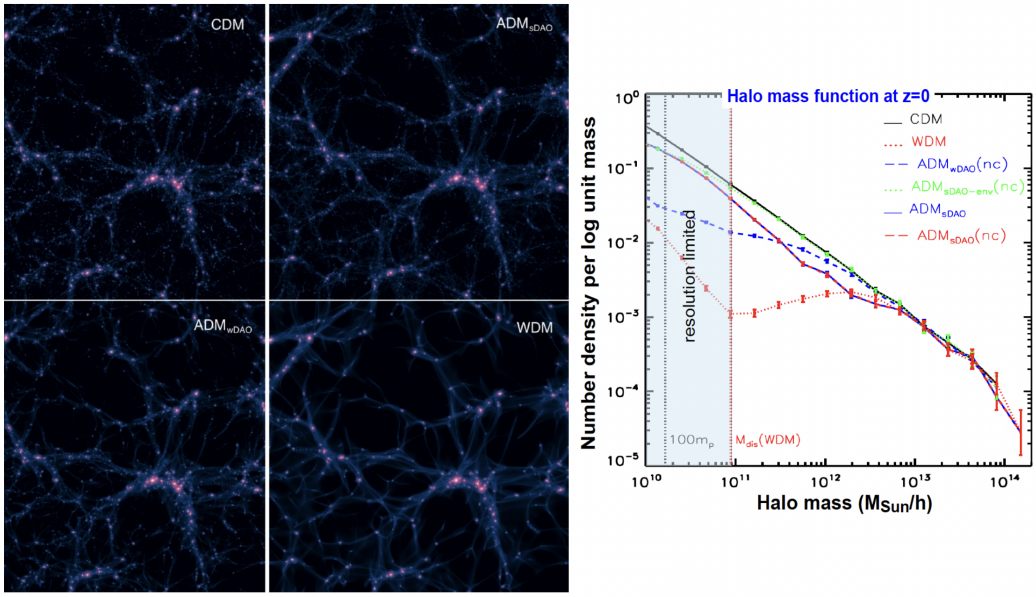

Figure 1.3: Halo mass function associated with different dark matter models from [Zavala & Frenk, 2019]. On the left, the large-scale dark matter distribution in a 64 Mpc/h cube in different cosmologies like CDM, WDM (Warm Dark Matter), and two other interacting dark matter models. The right figure shows the halo mass function at z = 0 for the models on the left figure. Credits: [Zavala & Frenk, 2019].

The [Navarro et al. 1996] work underlined two shortcomings proposed by the Cold Dark Matter (CDM) model: the halo of dwarf irregulars requires less concentrated CDM halos to have consistent results, and the predicted number of galaxy halos is way greater than the observed one. Most probably, core structures of the early dwarf galaxies were modified during their formation and subsequent evolution, giving an unsuitable comparison between the two kinds of halos. Moreover, it is possible that many galaxies did not form or remain undetectable in many dark matter halos.

The gravitational effect of dark matter and the rotation curve of spiral galaxies are the main proof of their influence. Following general theory, the rotational velocity of a galaxy should decrease at larger distances from the Galactic centre, but most of the observations of the 21cm line for neutral atomic hydrogen show a flat curve at larger distances, denoting that rotational velocities do not decrease as predicted. Considering that all visible matter was taken into account for observations, an unobservable matter was needed to explain these rotation curves, and it was originally proposed by K.C. Freeman in 1970.

Subsequent high-resolution N-body simulations from [Navarro et al. 1997] show that the shape of the density profiles of dark matter halos is independent of their mass, the initial density fluctuation spectrum, and the values of the cosmological parameters. In that framework, low-mass halos were significantly denser than more massive systems, implying a huge collapse redshift of small halos. Additionally, the density of the universe in which the halo was formed is proportional to the density of a halo at equilibrium.

Bulge and bar

The bulge is defined as a small stellar system that can be seen in the central region of the Galaxy. Representing about 15% of the overall luminosity of the Milky Way, it appears as a component thicker than the disk and perfectly visible in infrared images of the Galaxy, following [Zoccali et al. 2003] study. Stars in the bulge region are typically formed within the Galaxy itself, while stars belonging to other regions can have a wide range of ages (i.e. disk stars).

Usually, bulge stars have higher velocities than disk stars, with a velocity vector pointed towards random directions. They are covering a range of metallicity values that appears smaller for stars that can be found in the solar neighborhood, probably because the metal-rich debris from exploding supernovae has progressively polluted the interstellar gas required for disks star formation. According to the statistical relationship between temperature and mean-square velocity in a gas, the bulge population should have high temperatures since its random velocities are higher than the mean velocities.

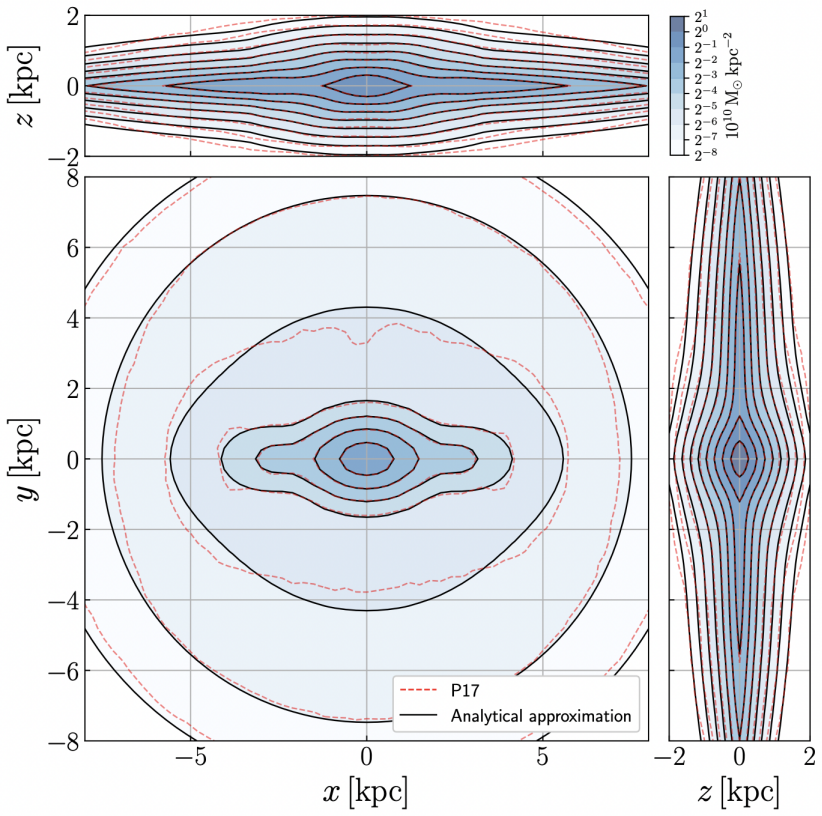

Figure 1.4: Best-fitting analytic model for surface density associated with time-averaged 3D density of the N-body model. Credits: [Sormani et al. 2022]

Even if the distribution of bulge stars appears symmetric, in reality, the bulge is brighter and thicker at positive Galactic longitudes (l >0). These features can be explained ac-

cording to the triaxial nature of the bulge (lengths of the two primary axes in the Galactic plane are in a 3:1 ratio), where the overall triaxial structure extends to around 3kpc from the centre; thus, the high brightness and thickness at positive longitudes of the bulge can be demonstrated because that side is closer to the Sun.

This asymmetry is one of the main reasons why bulges can be seen as actual Galactic bars.

In 1991, thanks to early studies from [Blitz & Spergel, 1991], first detailed dynamical models for the gas in the Galactic centre were defined based on the concept of a rotating bar. Originally, there was strong evidence from gas kinematics, but thanks to infrared observations, the existence of a galactic bar was confirmed.

Different views were proposed for the shape of the Galactic centre considering the latest infrared measurements, and according to [Binney et al. 1991] the centre of the Galaxy is shaped as a bar with a longer axis pointed towards the Sun. In the same work, the bar is described as having a triaxial peanut-shaped bulge. Different conclusions from central region observations give distinct metallicity populations, and in particular, near-infrared measurements can confirm the bulge and the bar components as two different structures in the large-scale infrared maps of the galaxy. At the time, the results described in both [Binney et al. 1991] and [Blitz & Spergel, 1991] works point to a bulge population of intermediate age that differs from the bar one.

It appears that there are two triaxial components in the Milky Way: the spheroid discussed in [Blitz & Spergel, 1991] was slowly rotating where its metal-poor population was positioned in the local neighborhood; then, the triaxial bulge was a metal-rich and fast rotating component; and these differences with spheroid components imply that the two systems had different formation histories. So, according to these early papers, the central triaxial components could be viewed as a peanut-shaped bulge or as a bar, and in the case of a rapid rotation highlighted by gas kinematics, these two views are equivalent: the edge-on view of a bar can be practically seen as a peanut-shaped bulge.

Results in [Blitz & Spergel, 1991] present an analytic model of the stellar mass distribution of the Milky Way bar, which can be seen in Fig. 1.4. Simulations were performed with an N-body model of P17 that reproduced the 3D density distribution, considering the inclusion of the central X-shaped.
One of the main results was a separation between *bar* and *long bar*, which has no physical meaning, but can actually be seen as a parameterization of the density distribution.

1.2 Merging events

Merging events between progenitor galaxies represent the baseline of describing the origin of the Milky Way halo: recent work by [Naidu et al. 2020] combines H3 Spectroscopic Survey and Gaia data in a 6D phase-space, with particular attention to the chemical information in the distant Galaxy regions. However, in both [Malhan et al. 2022] and [Malhan, 2022] studies, this result leads to a lack in the discussion of the dynamic parameters obtained from orbits around the galaxy, considering also the total number of mergers. The current work describes the cluster population associated with two specific and known merging events: Gaia-Sausage/Enceladus and the new Pontus event.

In the next sections, a brief description of various merging events is presented, alongside deeper insights on the Gaia-Sausage/Enceladus and Pontus events, with particular

attention to the importance of angular momentum along the z-axis, total energy, and eccentricity in an integrated orbit.

Meanwhile, in Section 2.1, the physical constraints of complex star systems will be discussed from [Binney & Tremaine, 2008] perspective, with a practical approach to the real-case rotating bar scenario related to [Naidu et al. 2020] and [Malhan et al. 2022] works.

Sagittarius, Sequoia, Thamnos and Cetus

Various events can be connected to the origin of the Milky Way, and in particular, they are not all mergers between progenitor galaxies. In the current context, some of these events will be described in the next sections.

Thanks to the [Ibata et al. 1994] discoveries on *Sagittarius* dwarf spheroidal galaxy (Sgr dSph), there is no doubt that the stream associated with the dwarf can highlight the hierarchical formation of the stellar halo of the Milky Way. With the upcoming early Gaia releases, much more complete sets of phase-space data have been used to provide more information about Sgr dSph, in accordance with [Minniti et al. 2021] description of the stream. Furthermore, [Naidu et al. 2020] confirmed intriguing properties of this dwarf spheroidal, such as high Sgr dSph energy, prograde overdensity in the E-L_z plane, and angular momentum concentration in L_y. Different peaks in [Fe/H] and a complex star formation history can underline populations with different chemical abundances. During the interaction between Sgr dSph and the Milky Way, the progenitor object was torn apart while sending oscillations (which can be seen as sound waves) all across the spiral arm structure. Remnants of the impact that produced the oscillations can be seen as dense and less dense star distributions above and below the Sun's position.

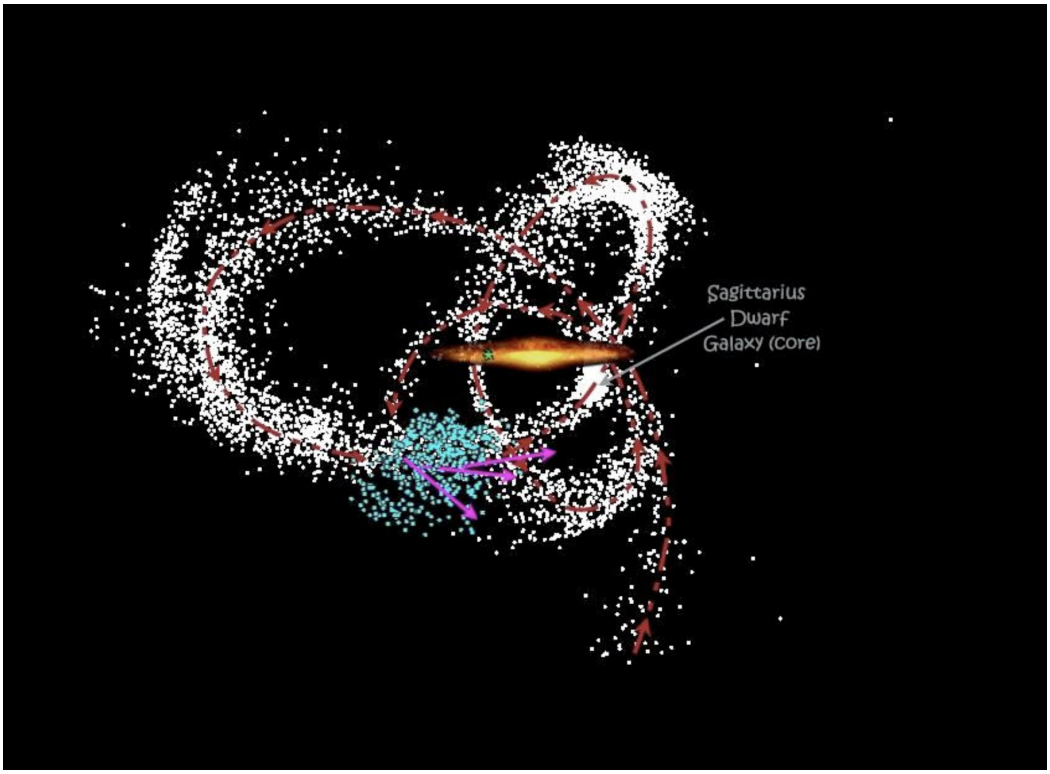

Figure 1.5: Sgr dSph is positioned face-on, so it is orthogonal to the plane of the Milky Way, superimposed with a Milky Way-like galaxy, and the position of the Sun is marked with a star. The dotted arrow represents the orbit of Sgr dSph. Credits: [Cole et al. 2010].

The *Sequoia* galaxy could also originate from merger debris, according to [Myeong et al. 2018]. The accretion process occurred approximately 9 Gyr ago, for which clustering methods returned five globular clusters linked to the Sequoia system, where seven other globular clusters were chosen from an energy-angular momentum selection: FSR 1758, NGC 3201, and NGC 6101 are common members of both selections, while IC 4499, NGC 5466, NGC 7006, and Pal 13 were excluded by the authors due to higher eccentricity compared to initial estimates. The Sequoia selection described could overlap with another debris proposed by [Helmi et al. 2018], and therefore, it is not fully possible to understand which is the progenitor of two members, NGC 3201 and NGC 6101, with proven age and metallicity; it is therefore possible to associate them with one particular event.

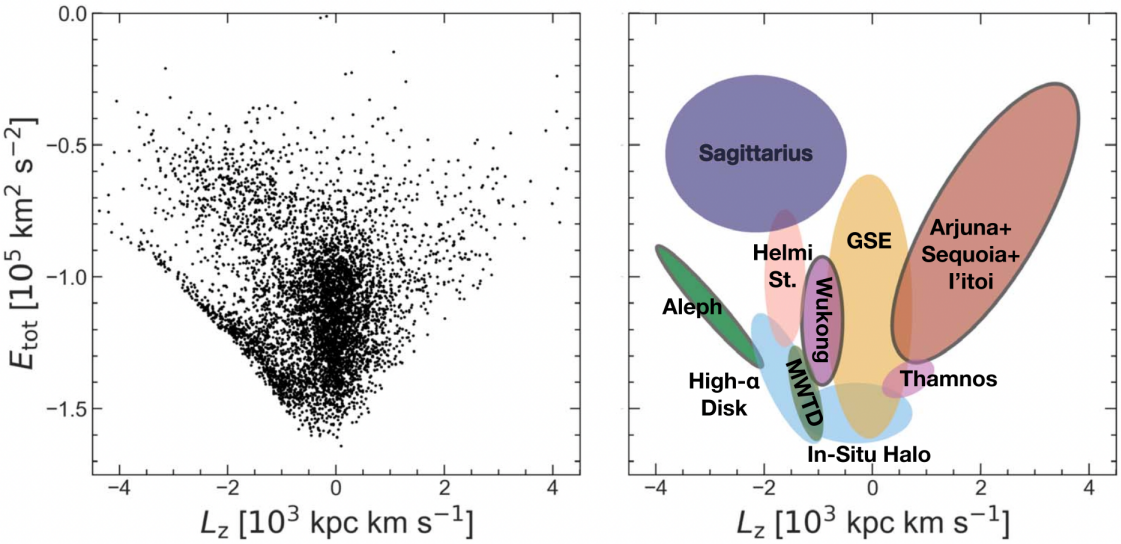

Figure 1.6: The general view of different structures in E-L_z plane where Gaia-Sausage/Enceladus, Sagittarius, Sequoia, and Thamnos can be recognised, with other structures like Wukong, Aleph, high-α disk, Arjuna/I'itoi, metal-weak thick disk (MWTD), and in situ halos. It is notable that most of the structures overlap one another. Credits: [Naidu et al. 2020].

Another interesting structure is represented by *Thamnos*, discovered in [Koppelman et al. 2018] from two overdensities called Thamnos 1 and Thamnos 2, assumed to have the same progenitor. These overdensities, according to [Naidu et al. 2020], can be seen in E-L_z diagrams along the edge of the Gaia-Sausage/Enceladus merger, which will be described in the following section, and it represents a single massive satellite that can produce different overdensities in E-Lz space . Thamnos and Gaia-Sausage/Enceladus differ, particularly on the chemical composition, considering the Thamnos stars studied by [Koppelman et al. 2018]. Therefore, Thamnos members can be selected from E and L_z values as previously described events, where some contamination by Gaia-Sausage/Enceladus can be found. Because of its low stellar masses, the Thamnos structure is an intriguing object, particularly because its debris can provide a unique perspective on stellar abundances and other parameters.

Following [Malhan et al. 2022], the *Cetus* group has one of the highest progrades of any detected group, and its members can be selected using an E-L_z selection. Cetus and Sagittarius members have similar values for E and L_z, but orbital properties and [Fe/H] values can be used to differentiate the two groups: in fact, Cetus members show a lower [Fe/H] than Sagittarius members. It is possible to estimate the mass of the progenitor galaxy Cetus thanks to the mass of one of its members, NGC 5824, obtaining $M_{halo} \sim 2 \cdot 10^{10} M_\odot$ and $M_\star \sim 3 \cdot 10^7 M_\odot$; due to the presence of many other streams for

Table 1.1: A summary of all angular momentum and total energy selections for Sagittarius, Sequoia, Thamnos, and Cetus. The values are taken from [Naidu et al. 2020] and [Malhan et al. 2022].

Name	Angular momentum [kpc km s^{-1}]	Total energy [km^2 s^{-1}]
Sagittarius	$L_y < -0.3L_z - 2.5 \cdot 10^4$	$-0.91 \cdot 10^5 < E < -0.79 \cdot 10^5$
Sequoia	$-3700 < L_\perp < -850$	$-1.5 \cdot 10^5 < E < -0.7 \cdot 10^5$
Thamnos	$0.2 \cdot 10^3 < Lz < 1.5 \cdot 10^3$	$-1.5 \cdot 10^5 < E < -1.3 \cdot 10^5$
Cetus	$2905 < L_\perp < 4635$	$-1.09 \cdot 10^5 < E < -0.93 \cdot 10^5$

which masses are not taken into account, these results are a strong underestimation of the true mass of the progenitor.

Gaia-Sausage/Enceladus merge

Accreted local halo can be associated with the Gaia-Sausage/Enceladus population, defined as GSE for simplicity. With the first releases from ESA's Gaia mission, it was possible to have many more confirmations of the early phases of the galaxy: [Belokurov et al. 2018] showed a significant amount of debris from Gaia Sausage, a minor merging event of a satellite galaxy, and Gaia Enceladus from [Helmi et al. 2018] work. Both events are treated as one main event, called collectively Gaia-Sausage/Enceladus, formed by 13 globular clusters plus 1 tentative association:

- NGC 7492
- NGC 6229
- NGC 6584
- NGC 5634
- IC 1257
- NGC 1851
- NGC 2298
- NGC 4147
- NGC 1261
- NGC 6981/M 72
- NGC 1904/M 79
- NGC 5904/M 5
- NGC 7089/M 2
- NGC 6864/M 75 (tentative)

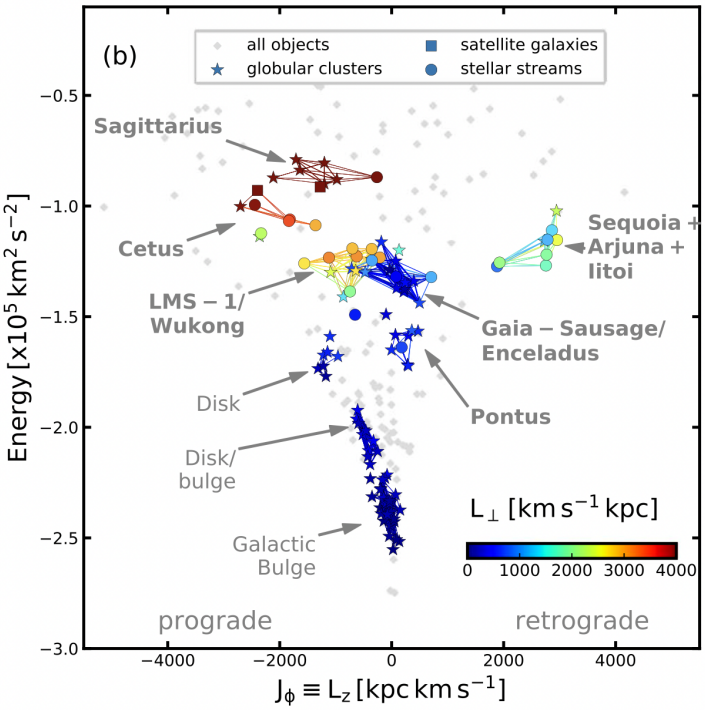

Figure 1.7: The J_ϕ vs. E plot for various structures (J_ϕ is the action along ϕ direction), with a contour map associated with L_z, where grey dots correspond to objects that do not belong to a specific merging event. If two objects show straight lines that connect them, these lines are associated with the frequency of these objects being members of the same group (a thick line means high frequency). Other structures are present compared to Figure 1.6, like Pontus, LMS-1, Cetus, disk, Galactic bulges, and disk/bulges. These lines are coloured using the same scheme as described above. This representation automatically reveals several independent groups. Credits: [Malhan et al. 2022].

According to [Naidu et al. 2020], [Mackereth et al. 2019], [Helmi et al. 2018], the GSE population contains high eccentricity objects (e $>$ 0.7), among which are stars with a wide range of chemical compositions compared to thick disk or halo stars, with [Helmi et al. 2018] and [Haywood et al. 2018] showing low [Fe/H] and high [α/H] abundances. This correlation was associated with the blue and red sequences of the main sequence in the Hertzsprung-Russel diagram, in the particular case of stars identified as halo stars because of their kinematics. This led to in situ formation for one population, while the other formed in other galaxies after merging with the Milky Way.

While explaining the higher metallicity of the red sequence compared to the blue sequence, numerical simulations In [Grand et al. 2020] confirmed that the blue sequence probably originates from an accreted dwarf galaxy, whereas the red sequence consists of stars formed in situ in the proto-disk of the galaxy, which were subsequently ejected towards the halo region after the merger. In addition, [Di Matteo et al. 2019] found that the high [α/H] sequence of halo stars also has high [Fe/H] abundances, close to thick disk populations, and that they are kinematically connected to each other.

Furthermore, high eccentricity values are strongly linked to a dense cloud of stars, with a density drop of around 30 kpc, according to [Lancaster et al. 2019]. As discussed in [Kim et al. 2021] paper, from metallicities, radial velocities, distances from SDSS-DR12 and proper motions from Gaia DR2, it is possible to separate objects with typical features of GSE into the so-called LOI and HOI subsample groups, where both show

highly eccentric and radial orbits. They particularly differ in eccentricity values (e< 0.9 for LOI, e> 0.9 for HOI) and variety of motion (prograde in inner halo and retrograde in outer halo). Both subpopulations are associated with two massive dwarf galaxies with prograde and retrograde orbits, with low inclination due to different dynamic friction and orbital directions.

In particular, HOI stars are viewed as being stripped from a massive dwarf galaxy by a high inclination orbit. Lastly, the [Kim et al. 2021] analysis implies that at least two low-mass progenitors are needed to explain the distinct properties between the LOI and HOI stars, which strongly characterised the origin of the GSE merger.

Pontus merge

A new merging event was recently discovered in the [Malhan et al. 2022] work while studying different mergers like Sagittarius, Cetus, GSE, LMS-1/Wukong, Arjuna/Sequoia/I'itoi. Characterised by low energy and slightly retrograde orbits, the new Pontus population currently consists of 7 globular clusters and 2 tentative associations (of which one was originally associated with the GSE event):

- NGC 288
- NGC 5286
- NGC 7099/M 30
- NGC 6205/M 13
- NGC 6779/M 56
- NGC 6341/M 92
- NGC 362
- NGC 7089/M 2 (tentative)
- NGC 6864/M 75 (tentative)

Moreover, the subsequent work of [Malhan, 2022] is focused on this new merging event, in which it was shown that the Pontus population has particular properties that are likely to originate from the merging of an independent satellite galaxy. Nevertheless, this extremely recent work needs more analysis to provide a much deeper insight into the overall group of merging events that could build the Milky Way. Like the GSE group, it is possible to find different kinds of objects that belong to Pontus, including a stream and seven clusters.

Two tentative objects, the NGC 6864 / M 75 globular cluster and the NGC 7089 / M 2, are classified as weak associations for [Malhan et al. 2022]. The energy values associated with Pontus members are close to those associated with GSE members, and, as a matter of fact, all Pontus globular clusters were previously associated with the GSE group. In Malhan's first work, there were some doubts regarding the actual separation between the two groups (i.e., the fragmentation process was neglected), but a much deeper study on dynamical properties showed interesting differences.

First, Pontus's candidate eccentricity was smaller than the one of GSE objects; because of that, GSE objects have more radial orbits and a higher average apocenter than the Pontus group members. Then, concerning velocities, the candidates GSE and Pontus showed distributions stretched along the R direction (radial orbits), while their velocity components along the ϕ direction differed; because of that, the Pontus objects seem

to have more retrograde orbits relative to the GSE objects, which have a much higher dispersion in V_ϕ. Also, the computation of the age-metallicity relation for both groups gives different behaviour, especially for metal-poor populations.
Using the Gaia dataset to analyse the phase-space distribution of Pontus members and the APOGEE dataset to examine their metallicity and chemical abundances, it was possible to define a precise chemo-dynamical analysis of the new population.

From [Malhan, 2022] results, the metal-poor and α-enhanced nature of the Pontus population implies an origin based on dwarf galaxy accretion. Furthermore, the origin of Pontus was observed to be approximately 5-6 Gyr ago. Considering that Pontus is more Mg-enhanced than Sagittarius and observations of Sagittarius, it is possible to assume that the Pontus galaxy accreted before Sagittarius: the population did not have enough time to be enriched in Fe through SN Ia, and therefore it ended up with more Mg and α elements. Likewise, these results are supported by the typical low-energy values of Pontus members, implying that the progenitor's accretion occurs very early in the time-evolution of the Milky Way.

According to the measured [Fe/H] abundances, it is probable that the Pontus progenitor was a massive system, approximately $10^7 M_\odot$. From color-magnitude diagrams, the Pontus population contains a double horizontal branch, where a few blue stragglers are present.

Table 1.2: The selection parameters used for GSE and Pontus candidates, where r_{per} and r_{apo} consist of the perigalacticon and apogalacticon radii, respectively, to find the closest and the farthest points to the galactic centre.

GSE	Total energy [km^2 s^{-2}]	$-1.6 \cdot 10^5 < E < -1.1 \cdot 10^5$
	Angular momentum along z-axis [kpc km s^{-1}]	$-0.5 \cdot 10^3 < L_z < 0.5 \cdot 10^3$
	Eccentricity	$e > 0.7$
Pontus	Total energy [km^2 s^{-2}]	$-1.72 \cdot 10^5 < E < -1.56 \cdot 10^5$
	Angular momentum along z-axis [kpc km s^{-1}]	$-470 \cdot 10^3 < L_z < 5 \cdot 10^3$
	Eccentricity	$0.5 < e < 0.8$
	Perigalacticon radius [kpc]	$1 < r_{per} < 3$
	Apogalacticon radius [kpc]	$8 < r_{apo} < 13$

The selection criteria used by [Horta et al. 2022], [Belokurov et al. 2018], [Haywood et al. 2018] and [Mackereth et al. 2019] for GSE and Pontus are listed in Table 1.2.

Therefore, thanks to the most recent studies [Malhan et al. 2022] and [Malhan, 2022], it is possible to conclude that Pontus and GSE are two distinct populations, mainly due to slightly younger globular clusters in the GSE population and different dynamic properties between them.

Chapter 2

Motion and potential components

Whether there are many confirmations of non-axisymmetric components, many real galaxies can be approximated as spherical systems. This chapter will describe the main points of interest associated with axisymmetric spherical potentials and non-axisymmetric potentials.

2.1 Axisymmetric spherical potentials

First, with the assumption of a symmetric potential with respect to the z-axis (so in the plane z=0) defined as $\Phi(R, z)$, the motion is governed by the Lagrangian:

$$\mathcal{L} = \frac{1}{2}[\dot{R}^2 + (R\dot{\phi})^2 + \dot{z}^2] - \Phi(R, z) \tag{2.1}$$

Taking into account that momenta are $p_R = \dot{R}$, $p_\Phi = R^2\dot{\Phi}$, and $p_z = \dot{z}$, the Hamiltonian will therefore be:

$$H = \frac{1}{2}\left[p_R^2 + \frac{p_\Phi^2}{R^2} + p_z^2\right] + \Phi(R, z) \tag{2.2}$$

To define the equations of motion, a set of generalized coordinates $\mathbf{q}$ and the generalized momentum $\mathbf{p}$ are introduced, and so the Hamiltonian will be:

$$p = \left(\frac{\partial \mathcal{L}}{\dot{q}}\right)_{q,t} \qquad \rightarrow \qquad H(q, p, t) = p \cdot \dot{q} - \mathcal{L}(q, \dot{q}, t) \tag{2.3}$$

It is possible then to rewrite the Hamiltonian in 2.2 and differentiate equation 2.3 to obtain:

$$dH = \left(\frac{\partial H}{\partial q}\right)_{p,t} \cdot dq + \left(\frac{\partial H}{\partial p}\right)_{q,t} \cdot dp + \left(\frac{\partial H}{\partial t}\right)_{q,p} \cdot dt \tag{2.4}$$

$$\begin{aligned} dH &= p \cdot d\dot{q} + q \cdot d\dot{p} - \left(\frac{\partial \mathcal{L}}{\partial q}\right)_{\dot{q},t} \cdot dq - \left(\frac{\partial \mathcal{L}}{\partial \dot{q}}\right)_{q,t} \cdot d\dot{q} - \left(\frac{\partial \mathcal{L}}{\partial t}\right)_{q,\dot{q}} \cdot dt = \\ &= q \cdot d\dot{p} - \left(\frac{\partial \mathcal{L}}{\partial q}\right)_{\dot{q},t} \cdot dq - \left(\frac{\partial \mathcal{L}}{\partial t}\right)_{q,\dot{q}} \cdot dt \end{aligned} \tag{2.5}$$

Thus, it can be noticed that in equation 2.5 the first and fourth terms in the first line are neglected due to the generalised momentum **p** defined in equation 2.3.
Equations 2.4 and 2.5 must be the same, therefore:

$$\dot{q} = \left(\frac{\partial H}{\partial p}\right)_{q,t} \quad ; \quad \left(\frac{\partial H}{\partial q}\right)_{p,t} = -\left(\frac{\partial \mathcal{L}}{\partial q}\right)_{\dot{q},t} \quad ; \quad \left(\frac{\partial H}{\partial t}\right)_{q,p} = -\left(\frac{\partial \mathcal{L}}{\partial t}\right)_{q,\dot{q}} \tag{2.6}$$

Using generalised **Lagrange equation**:

$$\frac{d}{dt}\left(\frac{\partial \mathcal{L}}{\partial \dot{q}}\right) - \frac{\partial \mathcal{L}}{\partial q} = 0 \tag{2.7}$$

Simplifying and rewrite the first two terms in 2.6 to obtain the Hamilton equations:

$$\dot{q} = \frac{\partial H}{\partial p} \qquad \text{and} \qquad \dot{p} = -\frac{\partial H}{\partial q} \tag{2.8}$$

Finally, **the equations of motion** can be derived from 2.8:

$$\begin{aligned} \dot{p}_R &= \ddot{R} = \frac{p_\phi^2}{R^3} - \frac{\partial \Phi}{\partial R} \\ \dot{p}_\phi &= 0 \\ \dot{p}_z &= \ddot{z} = -\frac{\partial \Phi}{\partial z} \end{aligned} \tag{2.9}$$

For an axis-symmetric system, these equations show the conservation of the angular momentum component along the z-axis ($p_\phi = L_z$, constant) and the coupled oscillations of the star in the R and z directions.

According to these results, an effective potential can be defined by using the constant value L_z. As a result, the three-dimensional motion in an axisymmetric potential $\Phi(R, z)$ can be reduced to a two-dimensional motion of the star in the (R,z) plane, also known as the meridional plane.

2.2 Non-axisymmetric potential: the bar issue

Non-axisymmetric structures may be seen towards the centre of many disk galaxies, where a bright stellar bar can be found. To correctly calculate galactic orbits, first we must understand how star orbits behave in a non-axisymmetric potential with bar component.

Assuming a static potential Φ, a rotating reference frame with an angular velocity Ω_b is chosen. In this frame, velocity is simply defined as $\dot{x}$; in the inertial frame, velocity is defined as $\dot{x} + \Omega_b \times x$.

The Lagrangian and the momentum can be written as:

$$\mathcal{L} = \frac{1}{2}|\dot{x} + \Omega_b \times x|^2 - \Phi(x) \qquad \text{and} \qquad p = \frac{\partial \mathcal{L}}{\partial \dot{x}} = \dot{x} + \Omega_b \times x \tag{2.10}$$

Moreover, substituting 2.10 results in the Hamiltonian will give:

$$\begin{aligned} H_J &= p \cdot \dot{x} - \mathcal{L} = \\ &= p \cdot (p - \Omega_b \times x) - \frac{1}{2}p^2 + \Phi = \\ &= \frac{1}{2}p^2 + \Phi - \Omega_b \cdot (x \times p) \end{aligned} \tag{2.11}$$

Recalling that the momentum in an inertial frame is denoted with p, then $x \times p$ is the angular momentum L and $\frac{1}{2}p^2 + \Phi$ is the Hamiltonian H in the inertial frame: so, it is possible to define a new Hamiltonian based on the inertial one. This new integral will be called the **Jacobi integral** and it will be defined as:

$$H_J = H - \Omega_b \cdot L \tag{2.12}$$

It is now easy to demonstrate that the quantity H inside the Jacobi integral and neither the angular momentum are conserved in a rotating non-axisymmetric potential.
Therefore, the Jacobi integral itself is conserved, and its constant value can be written from equation 2.11:

$$E_J = \frac{1}{2}\dot{x}^2 + \Phi - \frac{1}{2}|\Omega_b \times x|^2 \tag{2.13}$$

where $\Phi - \frac{1}{2}|\Omega_b \times x|^2$ is called effective potential Φ_{eff}.

Approach for rotating bar models

Following the [Naidu et al. 2020] approach, the variations in angular momentum along the z-axis and total energy seem to be neglected in a rotating bar model because of their smaller value with respect to the average value; so, a non-axisymmetric potential was treated as an axisymmetric one. In a more specific sense, the $\Omega_b \cdot L$ quantity shown in equation 2.12 is much smaller than the Hamiltonian in the inertial frame; therefore, the effective potential defined in equation 2.13 can be seen as equal to the static potential.

One of the primary goals of the WHVN algorithm is to integrate orbits according to two mass models that will be described in Chapter 4, and then compute various quantities such as the angular momentum along the z-axis L_z and the total energy E using a Monte Carlo approach for error propagation of both quantities.
The amount of variation of L_z and E over the integration time will determine whether the [Naidu et al. 2020] approach is actually consistent; if not, this difference must be taken into account, not only for dynamical purposes, but also to have a clear idea of the origin of a specific target in a merging event.

2.3 Possible outcomes

From a full population analysis that will be described later in Chapter 5, information regarding the target merger can be obtained, following [Naidu et al. 2020] work: it was shown that merging events group in specific regions of L_z-E plane, so the angular momentum along the z-axis and the total energy. Different orbital parameters were combined and used to select the members of each merger; in fact, the majority of the selections were based on angular momentum (L_z), total energy (E), and eccentricity (e). The [Naidu et

al. 2020] study was focused on different structures, like GSE and others, like high-α disk, in-situ halos (basically disk stars heated to eccentric orbits), Sagittarius merger (denoted as Sgr), the Helmi Streams, Sequoia, and Thamnos.

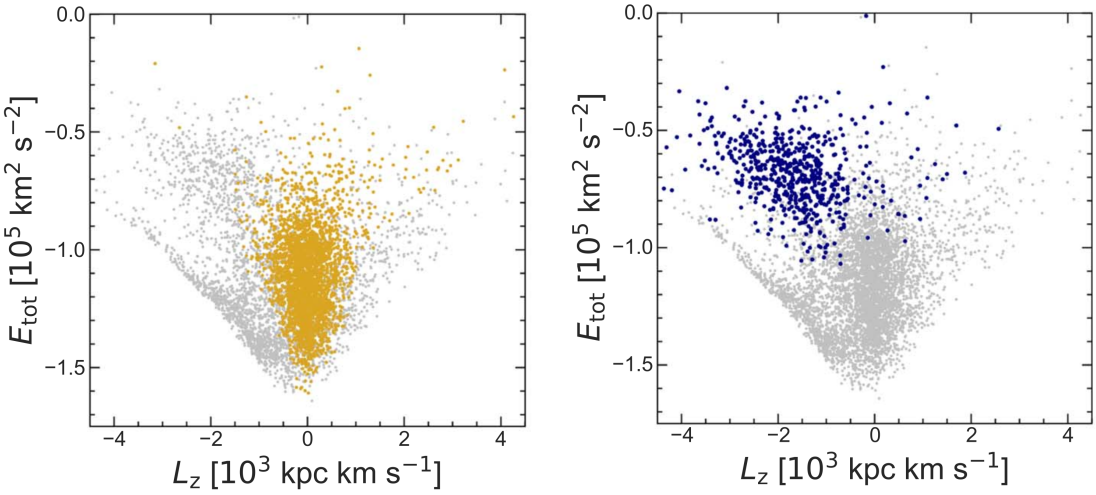

Figure 2.1: Gaia–Sausage/Enceladus and Saggittarius groups in L_z-E plots. Credits: [Naidu et al. 2020]

The results showed an arrangement that highlights a trend in these major orbital parameters: depending on the merging event, the globular clusters have specific values of L_z, E, and e. If so, it is possible to determine in which event a globular cluster formed and, therefore, which event can fully describe the origin of the Milky Way halo.
Results on GSE, in particular, show a trend for which low values of L_z are calculated, and E can vary within a certain range (Fig. 2.1). Following similar work from [Fu-Chi Yeh et al. 2020], GSE's high eccentricities are coupled with the small values of L_z (Fig. 2.2).

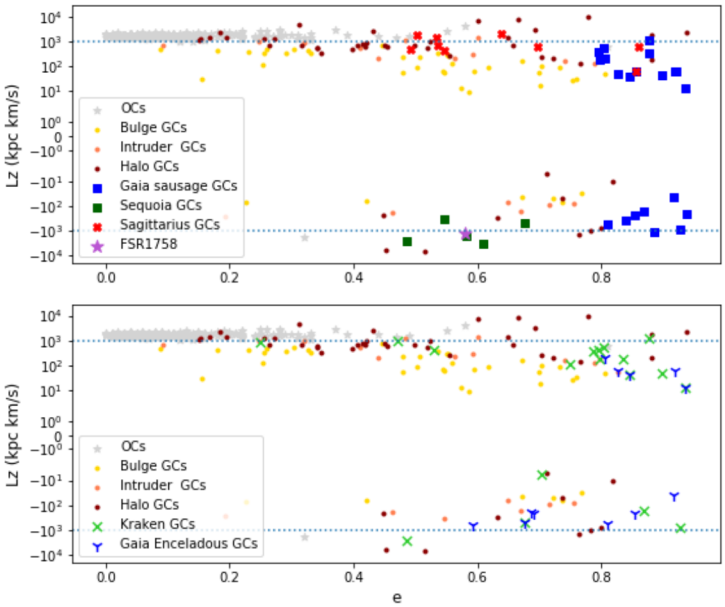

Figure 2.2: In the top image, globular clusters from Gaia-Sausage, Sequoia, and Sagittarius accretion events are compared with in situ globular clusters (GCs) and open clusters (OCs); in the bottom image, globular clusters from Kraken and Gaia-Enceladus events are compared with in situ GCs and OCs. Credits: [Fu-Chi Yeh et al. 2020]

On the other hand, insights on Pontus orbital parameters are quite rare in literature, due to its recent discovery. It is reasonable to expect Pontus members to arrange in some specific L_z-E-e ranges, and the current work (as well as future similar works) will try to shed light on a new player in the merging events discussion. Some early results can be found in the works of [Malhan et al. 2022] and [Malhan, 2022], where Pontus members arrange themselves in a specific region of the L_z-E plane.

When exploring [Naidu et al. 2020] and similar works, it is possible to notice that the L_z - E calculation lacks proper error propagation, but this is probably due to the high precision and accuracy of the integration processes and initial data, which result negligible errors to L_z, E, and population analyses.

Moreover, as described in 2.2, if a rotating bar is present, an oscillation of both Lz and E will occur; therefore, if oscillations in angular momentum and energy are small, one can define L_z and E as constant even if the bar is present. In order to display a fully consistent discussion, some approaches to the error issue will be presented in the current work, like the Monte Carlo error propagation for L_z and E, then scattering initial positions and velocities with a Gauss distribution, and finally quantifying the amplitude of oscillations in orbital parameters. Obviously, the previous discussion regarding the L_z-E-e connections will be taken into account too.

Chapter 3

Observational data

The WHVN calculates orbits using the typical Gaia mission dataset: celestial coordinates, distances, velocities along line of sight, and proper motions. This is possible thanks to a coordinate transformation into galactocentric coordinates that is implemented inside the WHVN code. In Section 3.1 the initial dataset and the idea behind the method are described, as well as the coordinate transformation method in Section 3.2. Then, the Gaia EDR3 used in WHVN can be found in Section 3.3.

3.1 Initial data, velocity and proper motions

Proper motion is defined as the angular velocity of a celestial body across the sky. Because of the great distances between the stars, only the nearest ones have proper motions big enough to be measured in arcseconds per year (or also milliarcseconds per year).
To measure appropriate movements, a telescope with a high angular resolution is required because of the modest angular velocities, and following the general outline of [Johnson & Soderblom, 1987] it is possible to use Gaia astrometric data to determine the proper motions. A similar work was carried out to measure the proper motion for 100 globular clusters by [Vasiliev, 2019] using Gaia DR2; then a comparison was subsequently made between his results and known proper-motion catalogues, and it was discovered that his data agreed well with [Gaia Collaboration, 2020] and the HST readings by [Sohn et al. 2018]. Proper motions are usually represented by μ and measured in arcseconds per year ("/yr). They can be seen as the sum of two components associated with right ascension and declination:

$$\mu^2 = \mu_\alpha^2 + \mu_\delta^2 \tag{3.1}$$

The ratio between proper motion and the star parallax gives the transverse velocity; in other words, we can obtain the velocity perpendicular to the line of sight (LOS) using the distances given by the Gaia parallaxes: following the radial velocity, this yields a three-dimensional space velocity of the observed object.

Following this outline, the Gaia EDR3 data from the studies of [Baumgardt & Vasiliev, 2021], [Vasiliev & Baumgardt, 2021] and [Vasiliev, 2019] was used in the current investigation. Phase-space coordinates of globular clusters in the Cartesian coordinate system centered on the Sun may be calculated by combining Vasiliev's proper motions of the GCs with the distances and line-of-sight velocities from [Harris, 2010]. According to this outline, Gaia EDR3 data were collected and converted into phase-space coordinates, resulting in initial position and velocities in a galactocentric coordinate system. Gaia EDR3 gives

celestial coordinates (α, δ) that must be converted into galactic latitude and longitude (l,b).

The chosen targets for the current study consist of 170 Galactic globular clusters and in particular, 20 of the nearest one were determined with an accuracy of 1% or even better. As can be seen from Gaia EDR3, it can be observed that for some globular clusters the velocity along the line of sight was not presented: these objects are still included in Table 3.2 to provide a complete image of the dataset, but they will not be processed by WHVN algorithm for computational purposes. The missing objects are as follows: Ko 1, Ko 2, Bliss 1, Kim 3, Ryu 059 / RLGC 1, Ryu 879 / RLGC 2, VVV CL002, Gran 1, and Pfleiderer 2. Note that these objects are not GSE or Pontus candidates and therefore, for the sake of the following work, the final results will not be affected.

In particular, they were added to [Vasiliev & Baumgardt, 2021] catalogue to reach a round and higher number of objects, where most of them represents recently-discovered globular cluster. The missing objects in Vasiliev's catalogue are poorly studied as of today's research (that's why line-of-sight velocity measurements are missing), and their nature is not well established. Further, in [Vasiliev & Baumgardt, 2021], it can be seen that a few of these objects have low Galactic latitudes and move within the disc plane: this implies a much more open cluster nature instead of a globular cluster one.
To simplify the final working code and reduce its computational load, GALA package from [Price-Whelan et al. 2017] gives the opportunity to use built-in functions to calculate the transformation from proper motions and distances to phase-space coordinates. With other AstroPy coordinate frames, it is possible to transform the initial Gaia EDR3 data into a Galactocentric frame to obtain the 3D positions and velocities. The details of the GALA transformation process will be discussed in the next section.

3.2 Coordinates transformation

As written in the previous section, to compute orbits in the proper manner, the Gaia EDR3 data must be converted in galactocentric coordinates and then in phase-space. GALA package is strongly based on AstroPy subpackages, as can be seen in GALA documentation that can be found in [Price-Whelan et al. 2017] and [Price-Whelan & Astropy Collaboration, 2018] papers.
The class *galactocentric_frame_defaults* was used in WHVN: this major class plays the role of controlling the global setting of all default values associated with the galactocentric frame. Different parameter settings can be used, and for the current work, the latest setting was used (april-may 2022). Then, GALA's galactocentric functions were coupled with other AstroPy subpackages, such as *astropy.units* and *astropy.coordinates*.

After inserting into WHVN the Gaia EDR3 data set, GALA built-in function (properly implemented in WHVN) rapidly converts all main parameters: right ascension α (in mas), declination δ (in mas), distance d (in kpc), the proper motions (μ_α and μ_δ, in mas/year) and the radial velocity (equal to the LOS velocity, in km/s). This will give both positions and velocities in Galactocentric coordinates ready to be used to integrate the target's orbit. The GALA built-in function is so implemented in the WHVN code to the user, that can insert initial parameters and work directly alongside the code, while the WHVN code associates the name of the target to each set of coordinates.

The combination of all data from [Baumgardt & Vasiliev, 2021], [Vasiliev & Baumgardt, 2021] and [Vasiliev, 2019], can be found in Table 3.2.
The starting point for Galactic dynamics and kinematics studies is represented by an

accurate estimate of the frame in which data is processed. The reference frame used is the Local Standard of Rest (LSR), as one can be found in [Price-Whelan & Astropy Collaboration, 2018] documentation. This frame consists of the mean velocity of the stars in the solar neighbourhood, which by general definition is described as follows: the LSR is the rest frame at the location of the Sun of a star that would be in a circular orbit (in the gravitational potential) one would obtain by azimuthally averaging away non-axisymmetric features in the actual Galactic potential.

Therefore, LSR represents the point in space that is moving on a perfectly circular orbit around the Galactic centre referred to the solar position. An accurate estimate of this group of parameters (i.e. peculiar velocities of the Sun) is the baseline of the conversion of the initial Gaia EDR3 dataset since all further calculations are made relative to the Sun. The estimation of galactocentric coordinates alongside the LSR parameters is based on the Oort constants for local spatial variations of the stellar velocity field, and orbital eccentricity distributions of different stellar populations (like globular clusters from different merging events) which can be used to investigate possible scenarios of Galaxy formation. The most important measurements are the three velocity components for the solar motion with respect to the LSR, represented collectively as $v_\odot = (U_\odot, V_\odot, W_\odot)$.

As we discussed in Chapter 1, such perfectly symmetric orbits cannot completely represent the real scenarios, but they can be used as a fair approximation for the velocity frame. Following the work of [Drimmel & Poggio, 2018] and [Shen et al. 2022], LSR parameters are presented in Table 3.1 based on the Sun position with respect to the Galactic Centre (GC).

Table 3.1: LSR parameters used for coordinates transformation.

Right ascension of the GC	$\alpha = 266.4051^\circ$
Declination of the GC	$\delta = -28.936175^\circ$
Distance from the Sun to the GC	$d_\odot = 8.122$ kpc
Height of the Sun above the Galactic plane	$z_\odot = 0.0208$ kpc
Motion of the Sun around the Galaxy	$v_\odot = (12.9, 245.6, 7.78)$ km/s

It has to be noted that the development of a stand-alone algorithm for coordinate transformation with Gaia EDR3 dataset (but also with all other Gaia releases) can be challenging. The amount of data and variables is extremely complex, and obviously hand calculations are highly time consuming. The choice of using the GALA and AstroPy packages to implement an algorithm that also contains the coordinate transformation was made because of these issues, especially if we want to compute more targets at the same time to display them all together. Therefore, thanks to the built-in GALA and AstroPy functions, it was possible to develop a simpler and lighter method that takes raw Gaia EDR3 and subsequently obtain more manageable parameters for galactic dynamics purposes. A more in-depth view of the WHVN algorithm and its features will be presented in Chapter 5.

3.3 Gaia EDR3

In the following section, the full data set of [Baumgardt & Vasiliev, 2021], [Vasiliev & Baumgardt, 2021] and [Vasiliev, 2019] from Gaia EDR3 is presented in Table 3.2. It refers to the main parameters used by the WHVN/GALA functions to obtain the phase-space coordinates: while right ascension α, declination δ, distance d, proper motions μ_α and μ_δ were introduced in the previous section, the parallax π is also noted in the table to be thorough.

The full Gaia Data Release 3 is divided into two main releases: the previously shown early release called Gaia Early Data Release 3 (Gaia EDR3) and the full Gaia Data Release 3 (Gaia DR3), that will probably be published during the first half of 2022.
As can be seen in Table 3.2 and following Gaia mission documentation from [Gaia Collaboration et al. 2020], the full dataset consists of positions on the sky (α, δ), parallaxes, and proper motions for 1.468 billion sources, taking a range of magnitudes in the G band between 21mag and 3mag. Additionally, there are cross-matches between Gaia EDR3 sources and other missions like the following: Hipparcos-2, Tycho-2 + TDSC merged, 2MASS PSC (merged with 2MASX), SDSS DR13, Pan-STARRS1 DR1, SkyMapper DR2, GSC 2.3, APASS DR9, RAVE DR5, allWISE, and URAT-1.

Table 3.2: Gaia EDR3 data is used, where objects with $\star$ symbol have missing data, as cited in Section 3.1, while some objects do not have errors in distance value.

Name	α [deg]	δ [deg]	d [kpc]	v_{los} [km s^{-1}]]	μ_α [mas yr^{-1}]	μ_δ [mas yr^{-1}]	π [mas]
Pal 1	53.333	79.581	11.18± 0.32	-75.72± 0.29	-0.2515± 0.0342	0.0075±0.0373	0.1118± 0.0226
Pal 2	71.525	31.381	26.17 ±1.28	-135.97± 1.55	10.448 ± 0.0341	-15.218± 0.0312	0.0420± 0.0212
Pal 3	151.383	0.072	94.84± 3.23	94.04± 0.80	0.0861± 0.0602	-0.1484± 0.0709	-0.0009± 0.0497
Pal 4	172.320	28.974	101.39± 2.57	72.40± 0.24	-0.1877± 0.0419	-0.4761± 0.0409	-0.0246±0.0326
Pal 5	229.019	-0.121	21.94± 0.51	-58.61± 0.15	-27.298± 0.0278	-26.540± 0.0272	0.0484± 0.0151
NGC 104 /47 Tuc	6.024	-72.081	4.52± 0.03	-17.45± 0.16	52.516± 0.0214	-25.515± 0.0214	0.2318± 0.0095
NGC 288	13.188	-26.583	8.99± 0.09	-44.45± 0.13	41.641± 0.0241	-57.053± 0.0243	0.1410± 0.0106
NGC 362	15.809	-70.849	8.83± 0.10	223.12± 0.28	66.935± 0.0245	-25.354± 0.0242	0.1141± 0.0105
Whiting 1	30.737	-3.253	30.59± 1.17	-130.41± 1.79	-0.2277± 0.0653	-20.458± 0.0561	0.0168± 0.0469
NGC 1261	48.068	-55.216	16.40± 0.19	71.34± 0.21	15.957± 0.0249	-20.642± 0.0251	0.0679± 0.0108
AM 1	58.760	-49.615	118.91± 3.40	118.00± 14.14	0.2912± 0.1071	-0.1772± 0.0859	-0.0124± 0.0602
Eridanus	66.185	-21.187	84.68± 2.89	-23.15± 0.73	0.5096± 0.0387	-0.3011± 0.0408	0.0503± 0.0327
NGC 1851	78.528	-40.047	11.95± 0.13	321.40± 1.55	21.452± 0.0240	-0.6496± 0.0242	0.0877± 0.0105
NGC 1904 / M 79	81.044	-24.524	13.08± 0.18	205.76± 0.20	24.690± 0.0249	-15.938± 0.0251	0.0879± 0.0109
NGC 2298	102.248	-36.005	9.83± 0.17	147.15± 0.57	33.195± 0.0255	-21.755± 0.0256	0.1213± 0.0110
NGC 2419	114.535	38.882	88.47± 2.40	-21.10± 0.31	0.0073± 0.0278	-0.5226± 0.0264	0.0025± 0.0166
$\star$ Ko 2	119.571	26.255	34.70		-0.5300± 0.1573	-0.0491± 0.1367	0.3734± 0.1602
Pyxis	136.991	-37.221	36.53± 0.66	40.46± 0.21	10.304± 0.0318	0.1378± 0.0347	0.0157± 0.0217
NGC 2808	138.013	-64.863	10.06± 0.11	103.57± 0.27	0.9944± 0.0238	0.2734± 0.0240	0.1121± 0.0103
E 3	140.238	-77.282	7.88± 0.25	11.71± 0.34	-27.274± 0.0272	70.827± 0.0271	0.1461± 0.0129
NGC 3201	154.403	-46.412	4.74± 0.04	493.65± 0.21	83.476± 0.0220	-19.575± 0.0221	0.2219± 0.0099
ESO 93-8	169.925	-65.220	13.70	86.00± 10.00	-40.679± 0.0329	14.002± 0.0338	0.1005± 0.0180
Crater	174.067	-10.877	147.23± 4.27	148.10± 0.65	-0.0585± 0.1254	-0.1157± 0.1161	0.0028± 0.1422
$\star$ Bliss 1	177.511	-41.772	23.70		-23.402± 0.0417	0.1378± 0.0382	0.0245± 0.0388
$\star$ Ko 1	179.827	12.260	48.30		-15.133± 0.1349	-0.8135± 0.1054	-0.0479± 0.1333
NGC 4147	182.526	18.543	18.54± 0.21	179.35± 0.31	-17.070± 0.0273	-20.896± 0.0274	0.0292± 0.0134
NGC 4372	186.439	-72.659	5.71± 0.21	75.59± 0.30	-64.090± 0.0241	32.975± 0.0238	0.1871± 0.0102
Rup 106	189.667	-51.150	20.71± 0.36	-38.36± 0.26	-12.535± 0.0264	0.4009± 0.0261	0.0672± 0.0129
NGC 4590 / M 68	189.867	-26.744	10.40± 0.10	-93.11± 0.18	-27.390± 0.0240	17.786± 0.0239	0.1132± 0.0106
BH 140	193.473	-67.177	4.81± 0.25	90.30± 0.35	-14.848± 0.0244	12.241± 0.0243	0.2188± 0.0105
NGC 4833	194.891	-70.877	6.48± 0.08	201.99± 0.40	-83.774± 0.0249	-0.9631± 0.0245	0.1635± 0.0106
NGC 5024 / M 53	198.230	18.168	18.50± 0.18	-63.37± 0.25	-0.1334± 0.0241	-13.306± 0.0240	0.0673± 0.0105
NGC 5053	199.113	17.700	17.54± 0.23	42.82± 0.25	-0.3293± 0.0253	-12.129± 0.0253	0.0500± 0.0114
$\star$ Kim 3	200.688	-30.601	15.10		-0.8620± 0.1686	33.412± 0.1305	0.0858± 0.1569

Name	α [deg]	δ [deg]	d [kpc]	v_{los} [km s^{-1}]]	μ_α [mas yr^{-1}]	μ_δ [mas yr^{-1}]	π [mas]
NGC 5139 / oCen	201.697	-47.480	5.43± 0.05	232.78± 0.21	-32.499± 0.0217	-67.463± 0.0216	0.1931± 0.0095
NGC 5272 / M 3	205.548	28.377	10.18± 0.08	-147.20± 0.27	-0.1519± 0.0228	-26.696± 0.0222	0.1104± 0.0102
NGC 5286	206.612	-51.374	11.10± 0.14	62.38± 0.40	0.1984± 0.0255	-0.1533± 0.0253	0.0883± 0.0109
AM 4	209.090	-27.167	29.01± 0.94	151.19± 2.85	-0.2911± 0.4448	-25.119± 0.3441	0.1074± 0.3366
NGC 5466	211.364	28.534	16.12± 0.16	106.82± 0.20	-53.423± 0.0245	-0.8223± 0.0242	0.0568± 0.0108
NGC 5634	217.405	-5.976	25.96± 0.62	-16.07± 0.60	-16.918± 0.0269	-14.781± 0.0263	0.0556± 0.0122
NGC 5694	219.901	-26.539	34.84± 0.74	-139.55± 0.49	-0.4636± 0.0293	-11.046± 0.0290	0.0335± 0.0171
IC 4499	225.077	-82.214	18.89± 0.25	38.41± 0.31	0.4658± 0.0253	-0.4890± 0.0253	0.0540± 0.0110
Munoz 1	225.450	66.969	45.00	-137.00± 4.00	-0.1031± 0.1920	-0.0591± 0.1792	0.2316± 0.1344
NGC 5824	225.994	-33.068	31.71± 0.60	-25.24± 0.52	-11.892± 0.0260	-22.338± 0.0257	0.0573± 0.0121
NGC 5897	229.352	-21.010	12.55± 0.24	101.31± 0.22	-54.217± 0.0252	-33.926± 0.0251	0.1047± 0.0110
NGC 5904 / M 5	229.638	2.081	7.48± 0.06	53.50± 0.25	40.856± 0.0230	-98.696± 0.0231	0.1409± 0.0101
NGC 5927	232.003	-50.673	8.27± 0.11	-104.09± 0.28	-50.564± 0.0246	-32.166± 0.0249	0.1271± 0.0105
NGC 5946	233.869	-50.660	9.64± 0.51	137.60± 0.94	-53.310± 0.0275	-16.572± 0.0271	0.1116± 0.0121
BH 176	234.781	-50.050	18.90	-6.00± 14.00	-39.889± 0.0293	-30.568± 0.0287	0.0719± 0.0178
NGC 5986	236.512	-37.786	10.54± 0.13	101.18± 0.43	-41.925± 0.0259	-45.680± 0.0256	0.1110± 0.0113
FSR 1716	242.625	-53.749	7.43± 0.27	-30.70± 0.98	-43.537± 0.0334	-88.318± 0.0312	0.1081± 0.0166
Pal 14	242.752	14.958	73.58± 1.63	72.30± 0.14	-0.4626± 0.0384	-0.4132± 0.0378	0.0355± 0.0323
Lynga 7 / BH 184	242.765	-55.318	7.90± 0.16	17.86± 0.83	-38.510± 0.0269	-70.495± 0.0271	0.1213± 0.0118
NGC 6093 / M 80	244.260	-22.976	10.34± 0.12	10.93± 0.39	-29.339± 0.0267	-55.784± 0.0261	0.1016± 0.0114
⋆ Ryu 059 RLGC1	244.286	-44.593	28.80		10.223± 0.0553	0.7697± 0.0470	-0.0658± 0.0463
NGC 6121 / M 4	245.897	-26.526	1.85± 0.02	71.21± 0.15	-12.514± 0.0231	-19.022± 0.0227	0.5558± 0.0099
NGC 6101	246.450	-72.202	14.45± 0.19	366.33± 0.32	17.558± 0.0241	-0.2577± 0.0245	0.0835± 0.0106
NGC 6144	246.808	-26.023	8.15± 0.13	194.79± 0.58	-17.435± 0.0263	-26.068± 0.0258	0.1315± 0.0114
NGC 6139	246.918	-38.849	10.04± 0.45	24.41± 0.95	-60.814± 0.0267	-27.112± 0.0262	0.1119± 0.0115
Terzan 3	247.167	-35.353	7.64± 0.31	-135.76± 0.57	-55.765± 0.0267	-17.597± 0.0261	0.1326± 0.0118
NGC 6171/ M 107	248.133	-13.054	5.63± 0.08	-34.71± 0.18	-19.392± 0.0253	-59.789± 0.0250	0.1943± 0.0108
ESO 452 / SC 11	249.854	-28.399	7.39± 0.20	16.37± 0.44	-14.234± 0.0314	-64.720± 0.0303	0.1621± 0.0150
NGC 6205 / M 13	250.422	36.460	7.42± 0.08	-244.90± 0.30	-31.493± 0.0227	-25.735± 0.0231	0.1269± 0.0102
NGC 6229	251.745	47.528	30.11± 0.47	-137.89± 0.71	-11.706± 0.0263	-0.4665± 0.0267	0.0405± 0.0116
NGC 6218 / M 12	251.809	-1.949	5.11± 0.05	-41.67± 0.14	-0.1914± 0.0241	-68.019± 0.0240	0.2078± 0.0105
FSR 1735	253.044	-47.058	9.08± 0.53	-69.85± 4.88	-44.395± 0.0537	-15.341± 0.0476	-0.0732± 0.0343
NGC 6235	253.355	-22.177	11.94± 0.38	126.68± 0.33	-39.306± 0.0272	-75.872± 0.0266	0.0895± 0.0122
NGC 6254 / M 10	254.288	-4.100	5.07± 0.06	74.21± 0.23	-47.577± 0.0235	-65.968± 0.0236	0.1959± 0.0103
NGC 6256	254.886	-37.121	7.24± 0.29	-99.75± 0.66	-37.149± 0.0312	-16.375± 0.0304	0.1621± 0.0126
Pal 15	254.963	-0.539	44.10± 1.14	72.27± 1.74	-0.5924± 0.0369	-0.9010± 0.0343	0.0239± 0.0247
NGC 6266 / M 62	255.303	-30.114	6.41± 0.10	-73.98± 0.67	-49.778± 0.0265	-29.467± 0.0263	0.1849± 0.0106
NGC 6273 / M 19	255.657	-26.268	8.34± 0.16	145.54± 0.59	-32.487± 0.0256	16.604± 0.0251	0.1419± 0.0107
NGC 6284	256.119	-24.765	14.21± 0.42	28.62± 0.73	-31.997± 0.0286	-20.021± 0.0278	0.0980± 0.0124
NGC 6287	256.288	-22.708	7.93± 0.37	-294.74± 1.65	-50.103± 0.0292	-18.830± 0.0277	0.1490± 0.0127
NGC 6293	257.543	-26.582	9.19± 0.28	-143.66± 0.39	0.8703± 0.0280	-43.260± 0.0275	0.1274± 0.0117
NGC 6304	258.634	-29.462	6.15± 0.15	-108.62± 0.39	-40.700± 0.0285	-10.878± 0.0283	0.1691± 0.0114
NGC 6316	259.155	-28.140	11.15± 0.39	99.65± 0.84	-49.691± 0.0313	-45.916± 0.0301	0.1129± 0.0135
NGC 6341 / M 92	259.281	43.136	8.50± 0.07	-120.55± 0.27	-49.349± 0.0243	-0.6251± 0.0239	0.1116± 0.0103
NGC 6325	259.497	-23.766	7.53± 0.32	29.54± 0.58	-82.893± 0.0302	-90.004± 0.0291	0.1621± 0.0134
NGC 6333 / M 9	259.797	-18.516	8.30± 0.14	310.75± 2.12	-21.801± 0.0262	-32.218± 0.0259	0.1351± 0.0109
NGC 6342	260.292	-19.587	8.01± 0.23	115.75± 0.90	-29.026± 0.0272	-71.156± 0.0265	0.1405± 0.0120
NGC 6356	260.896	-17.813	15.66± 0.92	48.18± 1.82	-37.501± 0.0264	-33.923± 0.0260	0.0957± 0.0119
NGC 6355	260.994	-26.353	8.65± 0.22	-195.85± 0.55	-47.384± 0.0312	-0.5721± 0.0301	0.1497± 0.0124
NGC 6352	261.371	-48.422	5.54± 0.07	-125.63± 1.01	-21.575± 0.0251	-44.465± 0.0247	0.1901± 0.0108
IC 1257	261.785	-7.093	26.59± 1.43	-137.97± 2.04	-10.069± 0.0400	-14.916± 0.0321	0.0568± 0.0274
Terzan 2 / HP 3	261.888	-30.802	7.75± 0.33	134.56± 0.96	-21.699± 0.0410	-62.626± 0.0382	0.1010± 0.0247
NGC 6366	261.934	-5.080	3.44± 0.05	-120.65± 0.19	-0.3324± 0.0246	-51.595± 0.0244	0.2852± 0.0107
Terzan 4 / HP 4	262.663	-31.596	7.59± 0.31	-48.96± 1.57	-54.616± 0.0600	-37.110± 0.0481	0.0897± 0.0407
HP 1 / BH 229	262.772	-29.982	7.00± 0.14	39.76± 1.22	25.228± 0.0391	-10.093± 0.0374	0.1243± 0.0143
FSR 1758	262.800	-39.808	11.09± 0.74	227.31± 0.59	-28.815± 0.0259	25.186± 0.0255	0.1223± 0.0112
NGC 6362	262.979	-67.048	7.65± 0.07	-14.58± 0.18	-55.058± 0.0238	-47.629± 0.0240	0.1358± 0.0104
Liller 1	263.352	-33.390	8.06± 0.34	60.36± 2.44	-54.028± 0.1087	-74.313± 0.0769	-0.0857± 0.0782
NGC 6380 / Ton 1	263.617	-39.069	9.61± 0.30	-1.48± 0.73	-21.832± 0.0310	-32.326± 0.0302	0.0988± 0.0144
Terzan 1 / HP 2	263.946	-30.481	5.67± 0.17	56.75± 1.61	-28.062± 0.0553	-48.613± 0.0548	0.0442± 0.0223
Ton 2 / Pismis 26	264.044	-38.553	6.99± 0.34	-184.72± 1.12	-59.041± 0.0308	-0.7551± 0.0294	0.1427± 0.0147
NGC 6388	264.072	-44.736	11.17± 0.16	83.11± 0.45	-13.159± 0.0262	-27.088± 0.0259	0.1001± 0.0113
NGC 6402 / M 14	264.400	-3.246	9.14± 0.25	-60.71± 0.45	-35.899± 0.0254	-50.588± 0.0255	0.1291± 0.0108
NGC 6401	264.652	-23.910	8.06± 0.24	-105.44± 2.50	-27.477± 0.0353	14.441± 0.0342	0.1489± 0.0131
NGC 6397	265.175	-53.674	2.48± 0.02	18.51± 0.08	32.603± 0.0227	-17.664± 0.0225	0.4165± 0.0098
⋆ VVV CL002	265.276	-28.845	8.00		-88.674± 0.1425	23.900± 0.0852	0.1398± 0.0992
Pal 6	265.926	-26.223	7.05± 0.45	177.00± 1.35	-92.219± 0.0384	-53.466± 0.0361	0.1036± 0.0168
NGC 6426	266.228	3.170	20.71± 0.35	-210.51± 0.51	-18.280± 0.0265	-29.992± 0.0265	0.0510± 0.0122
Djorg 1	266.868	-33.066	9.88± 0.65	-359.18± 1.64	-46.934± 0.0462	-84.678± 0.0411	0.0942± 0.0268
Terzan 5-11	267.020	-24.779	6.62± 0.15	-82.57± 0.73	-19.891± 0.0681	-52.433± 0.0661	0.1449± 0.0222
NGC 6440	267.220	-20.360	8.25± 0.24	-69.39± 0.93	-11.870± 0.0365	-40.196± 0.0351	0.1488± 0.0127
NGC 6441	267.554	-37.051	12.73± 0.16	18.47± 0.56	-25.514± 0.0283	-53.480± 0.0276	0.0833± 0.0113
Terzan 6 / HP 5	267.693	-31.275	7.27± 0.35	136.45± 1.50	-49.790± 0.0482	-74.313± 0.0392	0.0769± 0.0330
NGC 6453	267.715	-34.599	10.07± 0.22	-99.23± 1.24	0.2026± 0.0356	-59.336± 0.0368	0.0984± 0.0134
UKS 1	268.613	-24.145	15.58± 0.56	59.38± 2.63	-20.401± 0.0948	-27.541± 0.0633	0.0652± 0.0901

Name	α [deg]	δ [deg]	d [kpc]	v_{los} [km s^{-1}]]	μ_α [mas yr^{-1}]	μ_δ [mas yr^{-1}]	π [mas]
VVV CL001	268.677	-24.015	8.08± 1.48	-327.28± 0.90	-34.875± 0.1437	-16.523± 0.1075	0.1584± 0.1138
⋆ Gran 1	269.653	-32.020	8.80		-81.628± 0.0377	-80.453± 0.0364	0.0761± 0.0255
⋆ Pfleiderer 2	269.664	-5.070	16.00		-27.837± 0.0340	-41.576± 0.0313	0.0936± 0.0216
NGC 6496	269.765	-44.266	9.64± 0.15	-134.72± 0.26	-30.600± 0.0267	-92.711± 0.0261	0.1195± 0.0125
Terzan 9	270.412	-26.840	5.77± 0.34	68.49± 0.56	-21.211± 0.0517	-77.633± 0.0485	0.1555± 0.0169
Djorg 2 / ESO 456	270.455	-27.826	8.76± 0.18	-149.75± 1.10	0.6619± 0.0415	-29.828± 0.0371	0.1221± 0.0180
NGC 6517	270.461	-8.959	9.23± 0.56	-35.06± 1.65	-15.508± 0.0288	-44.698± 0.0282	0.1150± 0.0123
Terzan 10	270.742	-26.073	10.21± 0.40	211.37± 2.27	-68.266± 0.0594	-25.885± 0.0496	0.1455± 0.0445
NGC 6522	270.892	-30.034	7.29± 0.21	-15.23± 0.49	25.655± 0.0390	-64.384± 0.0358	0.1246± 0.0128
NGC 6535	270.960	-0.298	6.36± 0.12	-214.85± 0.46	-42.140± 0.0268	-29.387± 0.0265	0.1625± 0.0122
NGC 6528	271.207	-30.056	7.83± 0.24	211.86± 0.43	-21.571± 0.0432	-56.490± 0.0392	0.1246± 0.0182
NGC 6539	271.207	-7.586	8.16± 0.39	35.19± 0.50	-68.958± 0.0264	-35.374± 0.0260	0.1308± 0.0113
NGC 6540 / Djorg 3	271.536	-27.765	5.91± 0.27	-16.50± 0.78	-37.019± 0.0320	-27.911± 0.0318	0.1800± 0.0166
NGC 6544	271.836	-24.997	2.58± 0.06	-38.46± 0.67	-23.041± 0.0308	-18.604± 0.0305	0.3986± 0.0109
NGC 6541	272.010	-43.715	7.61± 0.10	-163.97± 0.46	0.2866± 0.0249	-88.472± 0.0245	0.1455± 0.0109
ESO 280 / SC 06	272.275	-46.423	20.95± 0.65	93.20± 0.34	-0.6878± 0.0392	-27.775± 0.0332	0.0411± 0.0257
NGC 6553	272.323	-25.909	5.33± 0.13	-0.27± 0.34	0.3445± 0.0301	-0.4538± 0.0295	0.1944± 0.0114
NGC 6558	272.573	-31.764	7.47± 0.29	-195.12± 0.73	-17.199± 0.0361	-41.438± 0.0337	0.1492± 0.0181
IC 1276 / Pal 7	272.684	-7.208	4.55± 0.25	155.06± 0.69	-25.531± 0.0258	-45.676± 0.0257	0.2099± 0.0113
Terzan 12	273.066	-22.742	5.17± 0.38	95.61± 1.21	-62.223± 0.0370	-30.524± 0.0336	0.1870± 0.0200
NGC 6569	273.412	-31.827	10.53± 0.26	-49.83± 0.50	-41.247± 0.0283	-73.543± 0.0279	0.1118± 0.0119
BH 261 / AL 3	273.527	-28.635	6.12± 0.26	-45.00± 15.00	35.656± 0.0434	-35.897± 0.0375	0.1929± 0.0225
NGC 6584	274.657	-52.216	13.61± 0.17	260.64± 1.58	-0.0898± 0.0258	-72.021± 0.0254	0.0773± 0.0114
Mercer 5	275.832	-13.669	5.50± 0.50	185.50± 3.75	-39.647± 0.1140	-72.199± 0.1106	0.2233± 0.0930
NGC 6624	275.919	-30.361	8.02± 0.11	54.79± 0.40	0.1245± 0.0292	-69.357± 0.0285	0.1304± 0.0120
NGC 6626 / M 28	276.137	-24.870	5.37± 0.10	11.11± 0.60	-0.2780± 0.0283	-89.222± 0.0280	0.2004± 0.0109
NGC 6638	277.734	-25.497	9.78± 0.34	8.63± 2.00	-25.185± 0.0287	-40.756± 0.0287	0.1148± 0.0122
NGC 6637 / M 69	277.846	-32.348	8.90± 0.10	47.48± 1.00	-50.339± 0.0276	-58.322± 0.0275	0.1160± 0.0117
NGC 6642	277.975	-23.475	8.05± 0.20	-60.61± 1.35	-0.1730± 0.0303	-38.922± 0.0300	0.1264± 0.0128
NGC 6652	278.940	-32.991	9.46± 0.14	-95.37± 0.86	-54.844± 0.0274	-42.739± 0.0268	0.1192± 0.0123
NGC 6656 / M 22	279.100	-23.905	3.30± 0.04	-148.72± 0.78	98.506± 0.0234	-56.175± 0.0232	0.3064± 0.0101
Pal 8	280.375	-19.826	11.32± 0.63	-31.54± 0.21	-19.871± 0.0270	-56.935± 0.0267	0.1151± 0.0124
NGC 6681 / M 70	280.803	-32.292	9.36± 0.11	216.62± 0.84	14.307± 0.0267	-47.438± 0.0261	0.1212± 0.0116
⋆ Ryu 879 / RLGC2	281.367	-5.192	15.80		-23.957± 0.0771	-17.940± 0.0692	0.0840± 0.0745
NGC 6712	283.268	-8.706	7.38± 0.24	-107.45± 0.29	33.629± 0.0270	-44.362± 0.0266	0.1464± 0.0112
NGC 6715 / M 54	283.764	-30.480	26.28± 0.33	143.13± 0.43	-26.792± 0.0253	-13.865± 0.0254	0.0532± 0.0111
NGC 6717 / Pal 9	283.775	-22.701	7.52± 0.13	30.25± 0.90	-31.253± 0.0273	-50.082± 0.0271	0.1174± 0.0120
NGC 6723	284.888	-36.632	8.27± 0.10	-94.39± 0.26	10.285± 0.0255	-24.185± 0.0254	0.1321± 0.0111
NGC 6749	286.314	1.901	7.59± 0.21	-58.44± 0.96	-28.293± 0.0276	-60.057± 0.0274	0.1380± 0.0116
NGC 6752	287.717	-59.985	4.12± 0.04	-26.01± 0.12	-31.611± 0.0225	-40.272± 0.0224	0.2544± 0.0098
NGC 6760	287.800	1.030	8.41± 0.43	-2.37± 1.27	-11.070± 0.0260	-36.150± 0.0262	0.1323± 0.0112
NGC 6779 / M 56	289.148	30.183	10.43± 0.14	-136.97± 0.45	-20.179± 0.0251	16.176± 0.0252	0.0910± 0.0107
Terzan 7	289.433	-34.658	24.28± 0.49	159.85± 0.14	-30.018± 0.0286	-16.510± 0.0287	0.0495± 0.0152
Pal 10	289.509	18.572	8.94± 1.18	-31.70± 0.23	-43.225± 0.0285	-71.728± 0.0286	0.1117± 0.0140
Arp 2	292.184	-30.356	28.73± 0.34	122.64± 0.29	-23.307± 0.0313	-14.753± 0.0294	0.0265± 0.0210
NGC 6809 / M 55	294.999	-30.965	5.35± 0.05	174.70± 0.17	-34.316± 0.0237	-93.110± 0.0237	0.2095± 0.0103
Terzan 8	295.435	-33.999	27.54± 0.42	148.43± 0.17	-24.958± 0.0270	-15.807± 0.0260	0.0499± 0.0130
Pal 11	296.310	-8.007	14.02± 0.51	-67.64± 0.76	-17.661± 0.0300	-49.709± 0.0284	0.1089± 0.0165
NGC 6838 / M 71	298.444	18.779	4.00± 0.05	-22.72± 0.20	-34.161± 0.0245	-26.559± 0.0244	0.2513± 0.0105
NGC 6864 / M 75	301.520	-21.921	20.52± 0.45	-189.08± 1.12	-0.5975± 0.0262	-28.099± 0.0258	0.0689± 0.0121
NGC 6934	308.547	7.404	15.72± 0.17	-406.22± 0.73	-26.545± 0.0260	-46.887± 0.0259	0.0778± 0.0118
NGC 6981 / M 72	313.365	-12.537	16.66± 0.18	-331.39± 1.47	-12.736± 0.0262	-33.608± 0.0257	0.0841± 0.0118
NGC 7006	315.372	16.187	39.32± 0.56	-383.47± 0.73	-0.1275± 0.0274	-0.6329± 0.0270	0.0349± 0.0149
Laevens 3	316.729	14.984	61.77± 1.65	-70.30± 0.82	0.1722± 0.1013	-0.6658± 0.0797	0.1296± 0.0880
Segue 3	320.379	19.117	29.50± 1.10	-167.00± 1.50	-0.9806± 0.1213	-16.668± 0.0807	-0.0051± 0.1168
NGC 7078 / M15	322.493	12.167	10.71± 0.10	-106.84± 0.30	-0.6588± 0.0239	-38.025± 0.0236	0.0968± 0.0104
NGC 7089 / M 2	323.363	-0.823	11.69± 0.11	-3.78± 0.30	34.346± 0.0247	-21.588± 0.0244	0.0824± 0.0107
NGC 7099 / M 30	325.092	-23.180	8.46± 0.09	-185.19± 0.17	-0.7374± 0.0246	-72.987± 0.0244	0.1360± 0.0108
Pal 12	326.662	-21.253	18.49± 0.30	27.91± 0.28	-32.197± 0.0291	-33.335± 0.0280	0.0502± 0.0177
Pal 13	346.685	12.772	23.48± 0.40	25.30± 0.22	17.475± 0.0487	0.1038± 0.0473	-0.0374± 0.0337
NGC 7492	347.111	-15.611	24.39± 0.57	-176.70± 0.27	0.7558± 0.0279	-23.200± 0.0276	0.0728± 0.0140

Chapter 4

Potential models

The first step in understanding the dynamics of the galaxy under different conditions is to define potential models associated with different galactic components such as a bulge, disk, halo, and rotating bar. In Chapter 3, phase-space coordinates were defined, such as position and velocities on the xyz axis.

It must be taken into account that most of the Milky Way's mass distribution is still unknown, due to observational constraints (i.e. dark matter). Moreover, as seen in Chapter 2, potentials and total energy conservation work differently if non-axisymmetric components are present. To present a full and legitimate description of this Milky Way dynamical study, more than one potential/mass model can be defined to reproduce the observational data.
Following [Irrang et al. 2013] study, two models can be defined that differ in the bulge potential chosen. These models share the same disk/halo configuration described by [Miyamoto & Nagai, 1975] and [Irrang et al. 2013].

Hereafter, the combination of the Navarro-Frenk-White dark matter halo model with the Miyamoto & Nagai approach for bulge and disk is denoted *Model I*. However, a spherical power-law density profile with an exponential cutoff model for the bulge is combined with Miyamoto & Nagai and Navarro-Frenk-White to define *Model II*, according to the data of [Bovy, 2015] work.

With no other components, these models perfectly describe an axisymmetric potential, for which the angular momentum and total energy should be constant. Nevertheless, this framework does not completely represent the real scenario, as mentioned many times before. As in most of the cases, a rotating bar represents the only non-axisymmetric component in the current study.

To fully describe such a component, the triaxial bar potential is given by [Long & Murali, 1992] in both Model I and Model II, often used in accordance with Miyamoto-Nagai potential for bulges and disks. In Figure 4.1, it is possible to see the rotation curve associated with both models: the behaviour is consistent for both models, considering that the attention is focused on globular clusters with orbit spread at no more than 30kpc from the Galactic centre. Therefore, a more detailed description of both models will be provided in the following sections.

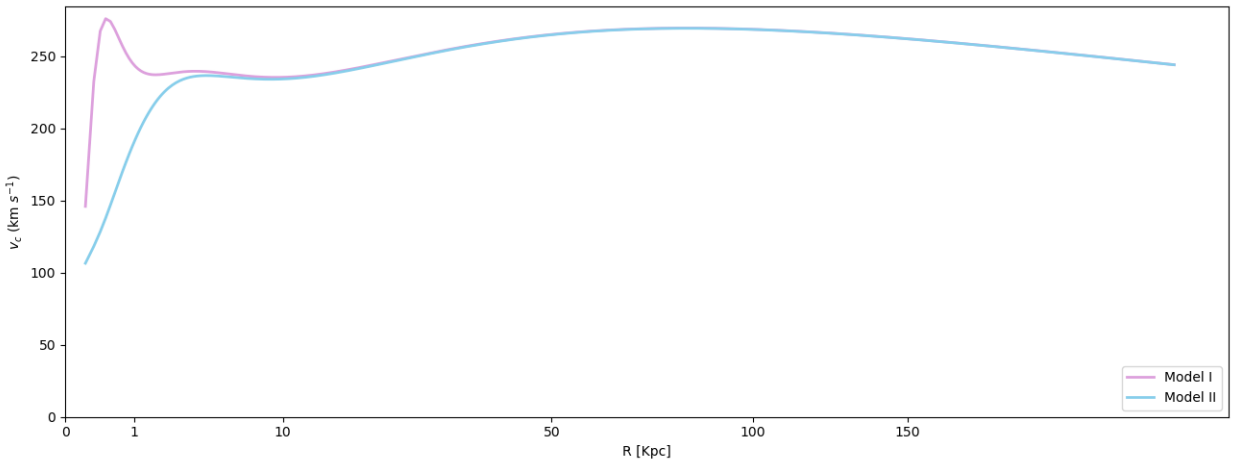

Figure 4.1: Rotation curves for Model I and Model II

4.1 Model I

Model I is probably the easiest and safest model to use, and it consists of three axisymmetric potentials for the bulge, disk, and halo, based on a revision of the [Allen & Santillan, 1991] potential from [Irrang et al. 2013].

Bulge and disk potentials were proposed by [Miyamoto & Nagai, 1975], where their masses M_b and M_d modulate their contribution together with their scale lengths b_b, a_d, and b_d:

$$\begin{aligned} \Phi_b(R) &= -\frac{M_b}{\sqrt{R^2 + b_b^2}} \\ \Phi_d(r,z) &= -\frac{M_d}{\sqrt{r^2 + (a_d + \sqrt{z^2 + b_d^2})^2}} \end{aligned} \tag{4.1}$$

Speaking of dark matter halo, the Navarro-Frenk-White profile is vastly used in galactic dynamics in accordance with simulations of collisionless dark matter particles, for lot of mass ranges and redshift values.

$$\rho_h(R) = \frac{M_h}{4\pi} \frac{1}{R(a_h + R)^2} \tag{4.2}$$

In NFW's density profile described in equation 4.2, the mass M_h is representative of the mass within a sphere of radius $R_{nfw} = 5.3a_h$, where a_h is the scale length of the halo. Due to the definition of the NFW density profile in 4.2, it can be seen that for $R \to \infty$ we obtain divergent total halo mass.

At this point, following [Navarro et al. 1997] and [Irrang et al. 2013], the potential used to describe the density profile of spherical dark matter halos is:

$$\Phi_h(R) = \frac{M_h}{R} ln\left(1 + \frac{R}{a_h}\right) \tag{4.3}$$

In the case of a rotating bar, the [Long & Murali, 1992] potential is introduced:

$$\Phi_{bar}(x, R) = \frac{M_{bar}}{2a} ln\left(\frac{x - a + T_-}{x + a + T_+}\right) \tag{4.4}$$

where the parameter $T_\pm$ depends on the dimensions of the bar (a,b,c):

$$T_\pm = [(a \pm x)^2 + y^2 + (b + \sqrt{(c^2 + z^2)^2}]^{1/2} \tag{4.5}$$

In Table 5.1 described in Section 5.2 of the next chapter, all the parameter values of the components are collected according to those that can be found in the [Bovy, 2015], [McMillan, 2017], [Navarro et al. 1997] and [Irrang et al. 2013] works.

The mass distribution of distinct components of the galaxy may be inferred from the orbits around itself. For example, as cited by [Irrang et al. 2013], the presence of dark matter in the Milky Way was originally suggested by star motion measurements; then, thanks to the Gaia mission and its high-accuracy data for stars, the orbits of stars were calculated using analytical mass models of the Galaxy.

Other models used from [Irrang et al. 2013] paper were based on [Allen & Santillan, 1991] and [Wilkinson & Evans, 1999] works. By employing observable constraints such as the Galactic rotation curve, distance to the GC, and local mass density, Allen developed a mass model that was updated beforehand with the latest observations, obtaining a halo that was limited by the outermost halo stars.

Besides, more models were defined in the Irrang paper, based on the flat rotation curve model of [Wilkinson & Evans, 1999] halo potential and another model derived from numerical cosmological simulations of [Navarro et al. 1997].

At Galactocentric distances higher than 15 kpc (where observational constraints are negligible and the halo component dominates), differences between models become notable because the halo presence becomes dominant.
Over the last 25 years, Navarro-Frenk-White halo mass distribution was widely used as a representative of the halo potential; this trend is fully also in the current paper, giving a secure and well-know baseline for mass distribution in the Milky Way.

Following [Long & Murali, 1992], a triaxial bar based on the Miyamoto-Nagai disk was defined from rearranging the gravitational potential of a uniform thin "needle", as the authors wrote.

Unlikely from other complex bar potentials, the triaxial one is defined from basic functions and determined by dimensionless parameters. As simple as it is, this potential is extremely effective for the current work.

4.2 Model II

The second model used is defined as a mere variation of the previous Model I in the bulge potential: bar, halo, and disk are represented with the same potential, respectively [Long & Murali, 1992], [Navarro et al. 1997] and [Miyamoto & Nagai, 1975].
This choice was made due to the vastly use of those potentials in literature to represent axisymmetric and non-axisymmetric systems, as can be seen especially in [Irrang et al. 2013] and [Bajkova et al. 2020].

Given these first assumptions, Model II is defined as Model I, but with a power-law density profile bulge that is exponentially cut-off. Such spherical potentials are derived from power-law density models in the form of the following:

$$\rho(r) = A\left(\frac{r_1}{r}\right)^{\alpha} e^{(r/r_c)^2} \tag{4.6}$$

where A is the amplitude applied to the potential that can be set as unity, α is the power of the exponential law, r_c is the cut-off radius and r_1 is a reference radius for the given amplitude.

These models were chosen based on the idea of treating two scenarios of different bulges, regarding the common origin of the bar, where the so-called boxy character of the bulge is usually given by an edge-on view of the bar. Most of the spirals have bars, mostly seen in the infra-red. As treated by [Athanassoula, 2005], galactic bulges probably formed due to bar instability in the inner disk.

In particular thanks to GalPy package (used by [Price-Whelan et al. 2017] to develop GALA package), it is possible to easily represent the Milky Way's gravitational potential with some built-in models: some of them are offered to simplify calculations, but they do not represent an accurate model for the Milky Way's gravitational potential.

A more accurate representation of the Milky Way on different scales was presented following [Bovy, 2015] line of thought: a bulge modelled as a power-law density profile that is exponentially cut-off was provided (power-law exponent and cut-off radius can be found in Table 5.1), followed by a Miyamoto-Nagai disk and an NFW dark-matter halo described in the previous section.

Other potential models could be used in the current discussion, such as the [Allen & Santillan, 1991], [Wilkinson & Evans, 1999], but also [Bajkova et al. 2020] and [Fu-Chi Yeh et al. 2020] as well. All of them have strong both theoretical and observational strengths, but they required additional parameters or constraints that can define the overall model in a much complex manner. Because of this, both Model I and Model II described in the current chapter were chosen as the simplest models to work on, that can provide proper data without computational strain the integration of the orbit.

For example, the constraint on the Allen halo potential in [Allen & Santillan, 1991] adds an intermediate comparison inside the code that slows down the integration; similar complications could appear using [Palous et al. 1993] bar potential. The aim of the WHVN code is to give a simple yet correct view of the Milky Way potential and globular clusters, and because the Model I and Model II defined represent the adequate approaches to the study of the current work.

Chapter 5

WHVN algorithm: development and functions

The WHVN algorithm by Andrea Cichellero is based on an Astropy-affiliated Python package named GALA by [Price-Whelan et al. 2017], that seeks to provide efficient tools for completing typical tasks in Galactic Dynamics research with flexible and user-friendly interfaces.
GALA provides the user with many tools that are often used in astrophysical coding: gravitational potentials and force assessment, orbit integration, dynamical coordinate transformations, and chaos indicators for non-linear dynamics.
In its standard configuration, this package uses units and astronomical coordinate systems defined in the AstroPy core package, such as *astropy.units* and *astropy.coordinates*.

The most important function is that the GALA package can also simplify the integration processes from a computational perspective: the main problem with often-used SciPy library is not object-oriented nature of its functions, usually inaccessible from the C language.
Additionally, GALA provides subpackages for different integration processes like Leapfrog integration scheme, but also high-order integration schemes such as the 5th order Runge-Kutta method (RK5) and Dormand-Prince method (DOPRI).

In the following sections, WHVN will be described in its entirety.

5.1 Potential implementation

GALA's *potentials* subpackage consists of several built-in potentials implemented in C and Cython language, plus base classes that allow the user to easily create new custom potential classes in pure Python language, or by writing custom C and Cython extensions. The strength of the GALA package is represented by how it creates a specific object to manage in a simpler way all the dynamical calculations. The most used object is the *orbit* object, that is a matrix with 6 columns and n rows, where n is the number of integrated points in the orbit trajectory. GALA allows the user to create *potential* objects that are fundamental for computing common galactic dynamical quantities referred to orbits, and because of that, it is often combined with the *integrate* and *dynamics* subpackages.

It is also possible to define a collection of reference frames that may be used for numerical integration of orbits in non-static reference frames, so that potential objects can be paired with a given reference frame and stored in a Hamiltonian object, which acts similarly to

the potential one.
This approach reduces the computational weight of numerical orbit integration and simplifies the usage of the final working code. In the initial tests of the WHVN algorithm, a custom integration algorithm based on Dormand-Prince method was written, but the computation of orbits for more than 1 Gyr required too much time, approximately 45 min for 1 Gyr orbit.

Following [Irrang et al. 2013], [Bajkova et al. 2020] and [Bovy, 2015] views of different models for the Milky Way described in Chapter 4, other potentials need to be created and imported inside the WHVN code because GALA consists of a few and very general potentials, so to describe the defined Model I and Model II, it was mandatory to implement GALA potential class. The implementation consists of the addition of the Miyamoto-Nagai bulge potential described in Section 4.1 because GALA's Miyamoto-Nagai potential refers only to the disk potential.

The 5th order Runge-Kutta scheme is also mandatory to fulfil the accessibility of the C/-Cython language for new custom potentials; this choice regarding the integration method will be consistent with our purpose due to the high accuracy of the RK5 scheme.

5.2 Integration and physical parameters

With the initial phase-space coordinates taken from Chapter 3, WHVN algorithm is capable of calculating potentials and computing a galactic orbit.

Input data must be in the form of a list of targets, whereas the name, positions, and velocities in the (x,y,z) space are given in columns.

According to the description in Chapter 4, the potential model must be specified for the integration process, *Model I* or *Model II*; also, it is possible to consider a rotating bar in each model.
The first value to be determined is *target*: it is an integer number and it shows which row is the reference target in the input file. Then, the code will read values for the selected target and associates them with the variables (name, positions and velocities) in the (x,y,z) space. So, for example, *target = 5* will use the fifth object as the starting reference target from the dataset file.

The next value to be determined is *number of orbits*: using the Gaussian distribution on initial position and velocities, the code can generate many scattered orbits according to the distribution. It can be useful to verify the contribution of random small perturbations on initial phase-space coordinates to the orbit and its parameters. By default, each scatter (on positions and velocities) is set to 0, but for different purposes can be easily set to different values.

Integration time (τ_{int} , given in Gyr) will be found specifying the *number of steps* (n) and the value of each *time-step* (dt), according to the formula:

$$\tau_{int} = n \cdot dt \tag{5.1}$$

Furthermore, all the physical quantities associated with different components of the galaxy (bulge, disk, halo, and bar) have to be specified before computing the orbit, taking into account that different models require different values of the same quantity (i.e. masses). The values considered for the components are taken from the [Bovy, 2015], [McMillan, 2017], [Navarro et al. 1997] and [Irrang et al. 2013] papers. For the bar potential, the

proportion given by [Pichardo et al. 2004] and data from [Bajkova et al. 2020] are used, with q_{bar} values as the length of the bar.

Masses are given as solar masses $M_\odot$, distances in kpc, and rotational speed in km s^{-1} kpc. Moreover, the gravitational constant G is set to unity. Values for different models can be seen in Table 5.1

Table 5.1: Parameters of the Galactic Potential for Models I and II

	Model I	**Model II**
M_{bulge} $[10^{10} M_\odot]$	1.02	0.89
M_{disk} $[10^{10} M_\odot]$	7.2	7.2
M_{halo} $[10^{10} M_\odot]$	330.6	330.6
M_{bar} $[10^{10} M_\odot]$	1	1
b_b, r_c [kpc]	0.236	2.10
a_d [kpc]	3.262	3.262
b_d [kpc]	0.289	0.289
a_h [kpc]	45.02	45.02
q_{bar} [kpc]	8	
Ω_{bar} [km s^{-1} kpc]	31, 41, 55, 70	
$a_{bar} : b_{bar} : c_{bar}$	10 : 3.75 : 2.56	

Due to the presence of the bar, the potential must be associated with the speed of rotation of the bar (that is, the entire potential rotates with the speed of the bar).

All potentials except bar are axisymmetric in this framework: assuming a rotating bar around the z-axis with Ω_{bar}, the code generates a Hamiltonian object with a constantly rotating reference frame with this frequency. In addition, it is also possible to estimate the rotational velocities for all galactocentric radii and the position of the corotation resonance, but this will not be discussed in this work.

As previously mentioned, it is possible to draw random samples from a normal (Gaussian) distribution applied to all particles at initial positions and velocities.

The input parameters associated with the normal distribution are the initial values of the phase-space and the standard deviation (spread, or "width"), which must be positive or equal to 0. The standard deviation for both position and velocity is set to default at 0.

The integration of orbits is referred to as a non-inertial system, where mean positions and velocities are connected to the rotation of the bar. After the integration of the non-inertial orbits, it is possible to move to an inertial system thanks to a built-in class of GALA package.

5.3 Main functions

After the integration, the resulting output of the WHVN code is represented by the positions and velocities of the test particle in the galactic potential defined over the integration time. In GALA and so in WHVN, this output is represented by an *orbit* object that can be used with other classes to determine useful parameters or representations of the data.

The current study on merging events candidates is based on some interesting functions, which will be described in the current section. In addition, error propagation will be performed following Monte Carlo methods to confirm or deny the resulting data.

2D and 3D orbit representation

The functions *orbits()* and *orbit3D()* will represent the position of the test particle during the integration time on different axes. More specifically, *orbits()* will give positions along three planes in (x,y) , (x,z), and (y,z), while *orbit3D()* gives a three-dimensional interactive plot in the space (x,y,z). In Figure 5.1 and Figure 5.2 the orbit of the well-known globular cluster Palomar 5 is integrated with Model I, defined in Chapter 4.

These functions can be extremely useful to understand whether the integrated orbit is consistent: proximity to the bulge (x,y,z→0), size, and symmetry of the integrated orbit must be checked before proceeding with other calculations.

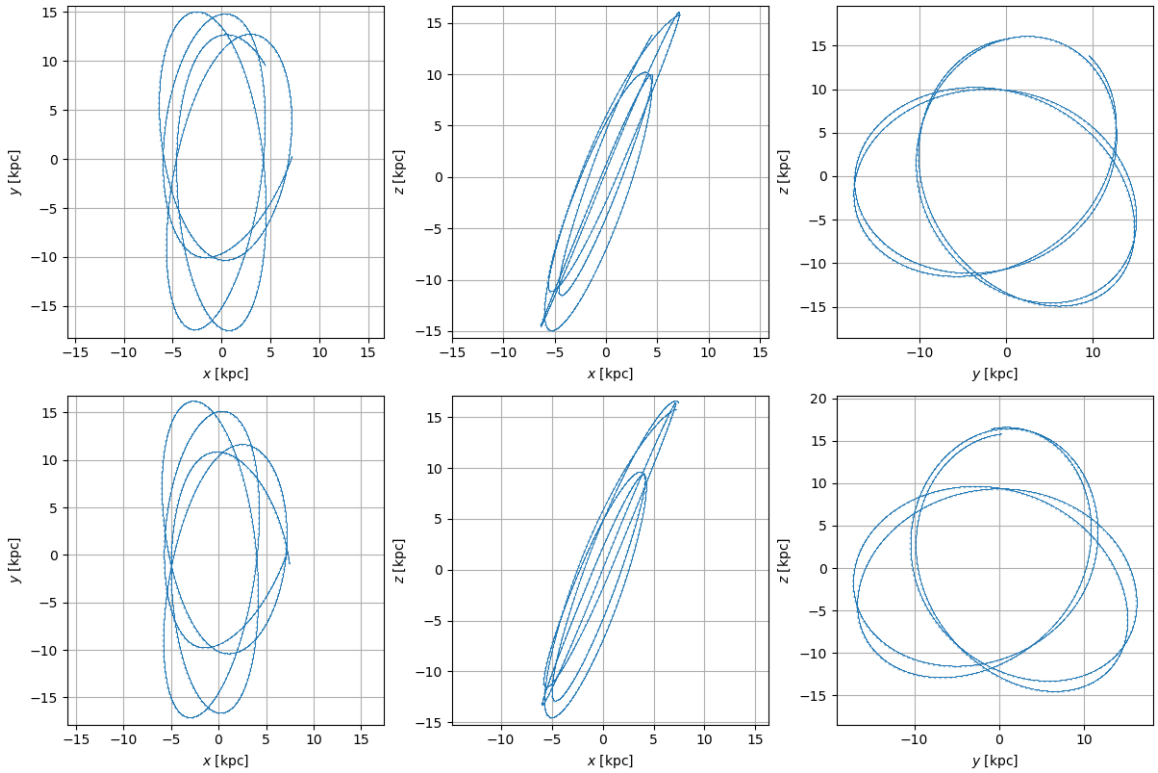

Figure 5.1: Pal 5 orbit in three 2D planes integrated with Model I (1.5 Gyr of integration time, with 15000 steps of 0.1 Myr): (up) bulge, disk and halo; (down) with rotating bar.

In the real-case scenario, stars whose movements take them outside of the system's equatorial plane are interesting regarding orbit integration. By using the conservation of the azimuthal angular momentum of each star, the study of such general orbits in axisymmetric galaxies may be simplified to a two-dimensional issue, leading to the so-called

meridional plane representation.

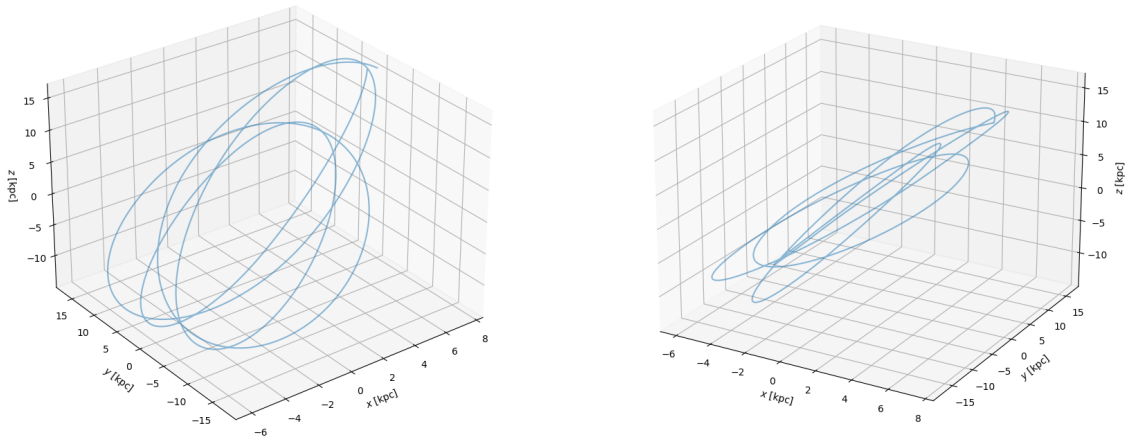

Figure 5.2: Pal 5 orbit in an interactive 3D space with different orientations, integrated with Model I (1.5 Gyr of integration time, with 15000 steps of 0.1 Myr) with rotating bar.

Thanks to GALA package, it is possible to visualise the orbit in just one projection of some transformed coordinate representation, like cylindrical radius ρ and z. In WHVN, the function *mer_plane()* will give a two-dimensional representation of the three-dimensional integrated orbit: for example, in Figure 5.3, the result of this function for NGC 362, integrated with Model II, can be seen.

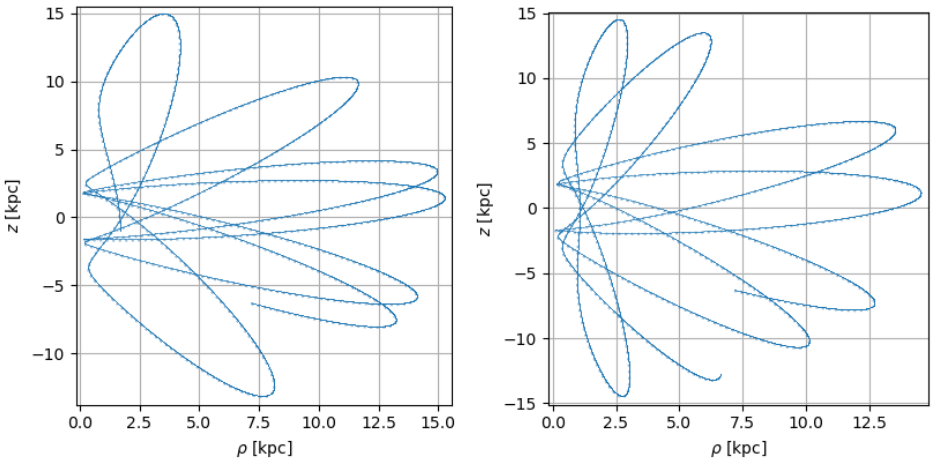

Figure 5.3: NGC 362 (ρ,z) plane, integrated with Model II (1.5 Gyr of integration time, with 15000 steps of 0.1 Myr): (left) bulge, disk and halo; (right) with rotating bar.

Unfortunately, most galaxies have at least one non-axisymmetric component, such as a luminous stellar bar (i.e. the Milky Way), and so it is safer to discuss these potentials with the same visual representation in order to understand how stars orbit in a non-axisymmetric potential behave.

Angular momentum over z-component and total energy

The GALA package provides a simple function to calculate angular momentum and energy from an *orbit* object. These built-in functions reduce computational weight and can be used to create a graphical representation of the angular momentum along the z-component L_z and the total energy E over the integration time.

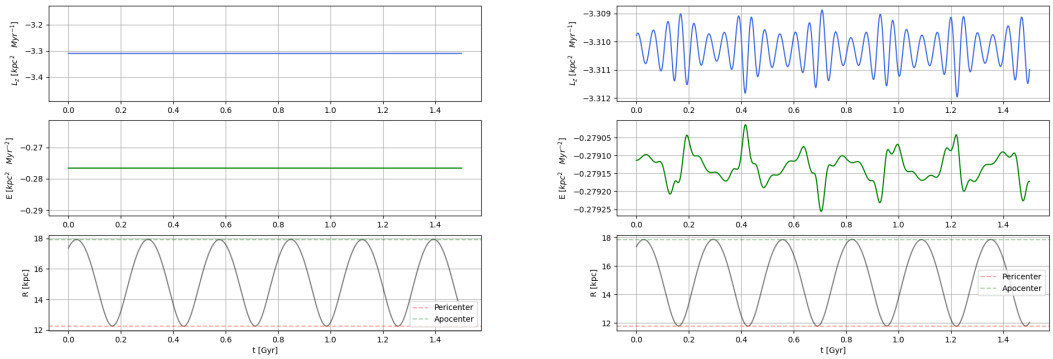

Figure 5.4: Angular momentum and total energy variation over time for Pal 3, integrated with Model I (1.5 Gyr of integration time, with 15000 steps of 0.1 Myr) with no rotating bar.

This is visible thanks to the *lz_e()* function developed in WHVN, which shows the variation of L_z and E over the integration time during the orbit, and thus whether these two quantities will be constant or not. Furthermore, the variation of distance during the interaction was represented, to check at which specific values of the radius the variations of L_z and E can be found. Figure 5.4 shows how the bar component can actually affect both the angular momentum and the total energy values. Constant values of L_z and E are encountered if there is no bar component; moreover, with a bar component, both values should vary, as discussed in Chapter 1.

As a result, the conservation of L_z and E can be verified using the *lz_e()* function.

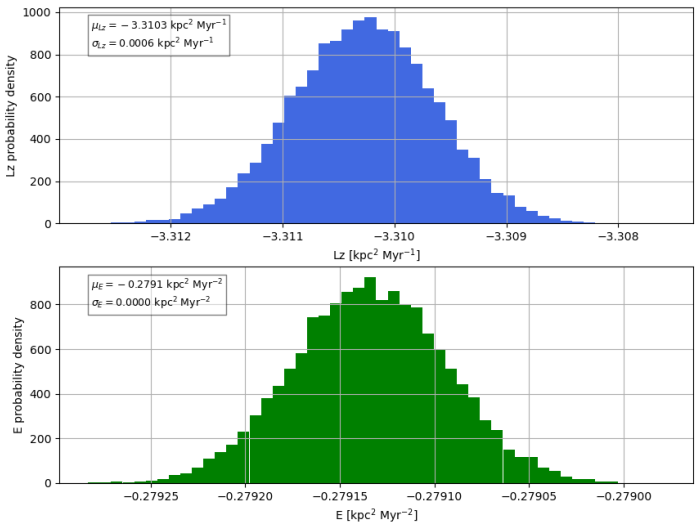

Figure 5.5: Monte Carlo error propagation associated to 5.4, where μ is the central value of L_z or E, and σ the standard deviation truncated after the fourth digit.

The function *lz_e()* gives another output: if there is a variation of L_z and E, due to a Monte Carlo approach associated with a normal distribution, it can check the propagation of the error with respect to the oscillations of the integrated values of both parameters, as seen in Figure 5.5.

Population analysis function

Following [Naidu et al. 2020] paper, a fundamental tool to describe the belonging to a particular merging event is to compare values of L_z and E for a specific population. In Naidu's work, according to [Malhan et al. 2022] and [Malhan, 2022], globular clusters collocate themselves in particular regions according to the event in which they originated.

In the current context, an analysis of the Gaia EDR3 dataset provided by [Baumgardt & Vasiliev, 2021] and [Vasiliev & Baumgardt, 2021] will be done with an eye open to Pontus and GSE mergers. In order to verify Naidu's results, an average value of L_z and E is taken, considering the small oscillations in these parameters. All of this is possible thanks to *compare_pop()* function provided in WHVN, as can be seen in Figure 5.6.

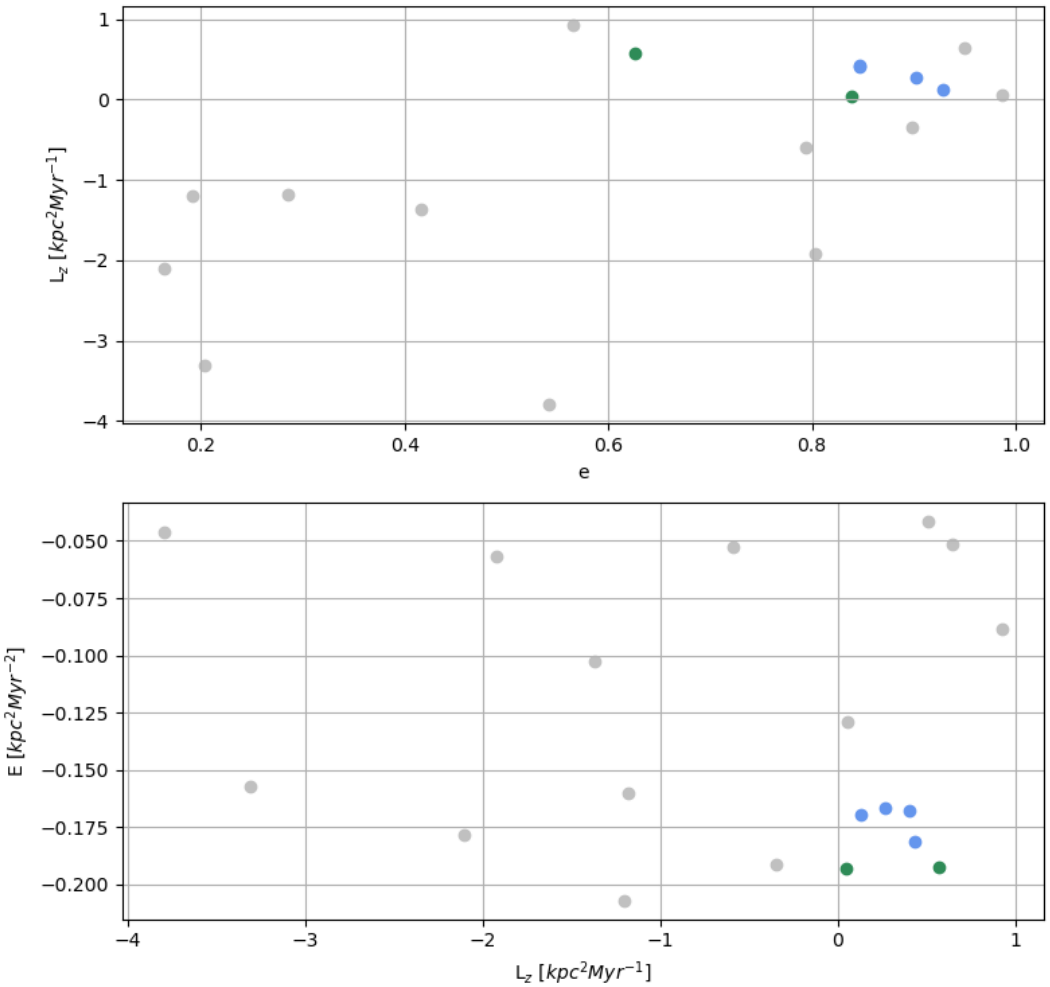

Figure 5.6: Test for *compare_pop()* function. Some targets can be highlighted with different colours depending on the purpose. In the above plots: grey dots represent cluster not associated with GSE or Pontus; green ones are Pontus candidates; blue one are GSE candidates

Other functions

The WHVN algorithm is implemented with other functions that can help to understand the structure of the potential influence of the Milky Way over orbiting objects.

Equipotential lines can be useful to describe how each component can affect the shape of the gravitational interaction within a certain distance from the centre of the potential. This type of plot shows the value of a potential in a two-dimensional grid in a plane thanks to a contour map. The *equipot()* function presented in WHVN shows exactly the behaviour of the potential in three different planes, (x,y) , (x,z), and (y, z), as seen in Figure 5.7; switching on/off some of the components can show the real shape of a single (or the total) potential, and so, if the behaviour of the orbits is consistent with mass distributions.

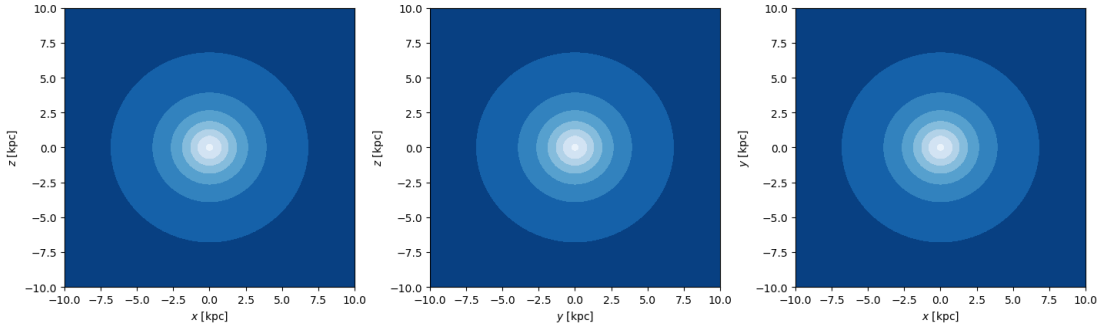

Figure 5.7: Test for *equipot()* for bulge potential in Model II.

If WHVN is implemented with new models, *rot_curve()* can plot the rotation curve for the new model, as long as previously discussed Model I and Model II in Chapter 4.

The function *vel_var()* is an implementation of *lz_e()* that was previously discussed; the main difference is the representation of the values of the velocity projections during the orbit. This can be useful to understand the physics behind different shapes of Lz or E variation over time plots, as can be seen in Figure 5.8.

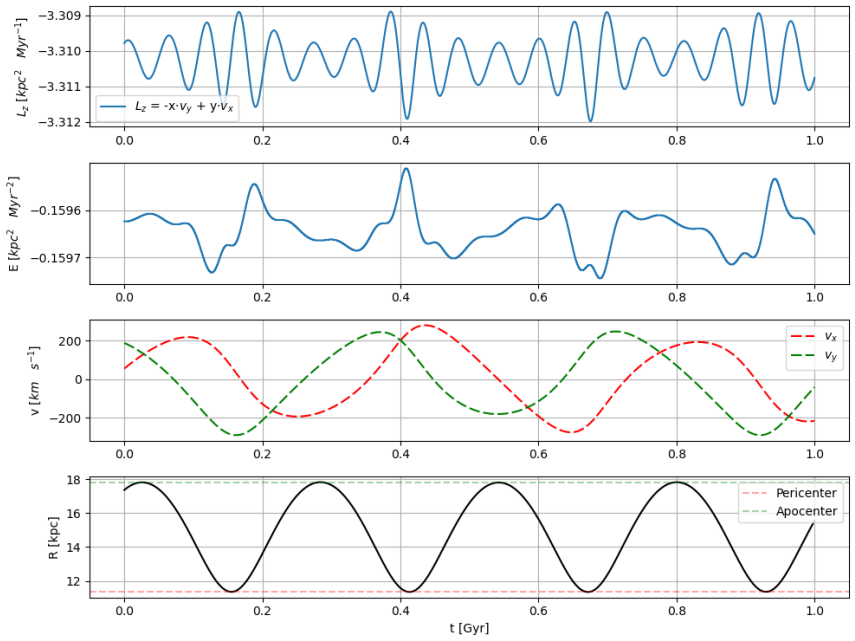

Figure 5.8: Test plot for *vel_var()* function for Model I.

Chapter 6

Results

In the current chapter, results from different functions of WHVN will be presented: most of the comparisons will be made regarding both Model I and Model II defined in Chapter 4, in the presence or absence of a rotating bar (as discussed in Section 2.2), and using cluster candidates for both GSE and Pontus events discussed in Chapter 1.

6.1 Equipotential lines

In order to properly understand the influence of each potential component and also check if the potential used is consistent with theoretical assumptions, it is useful to compute equipotential lines; they consist of 2D-countour plots, where spatial coordinates are along the x and y axis, while a colour gradient highlights different potential influences. The *equipot()* function developed within the WHVN code is used to present equipotential lines for each component and the entire system, for both Model I and Model II, in figures 6.1, 6.2, and 6.3.

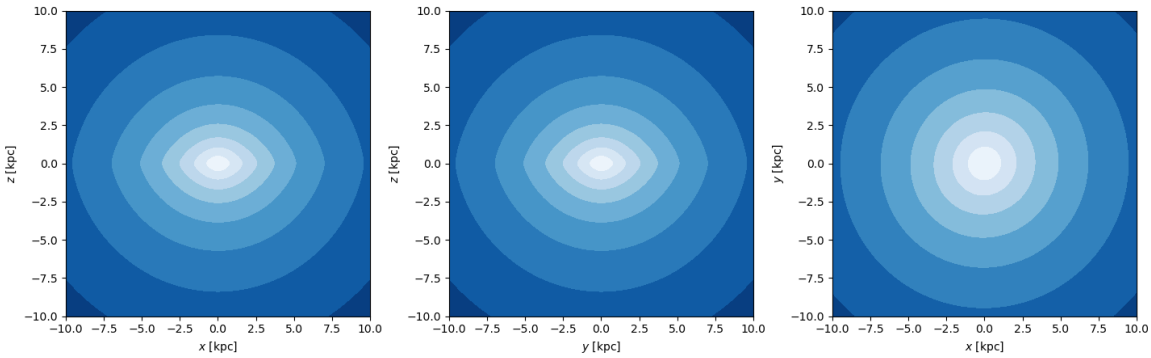

Figure 6.1: Equipotential lines for the total potential used for Model I, with Miyamoto-Nagai bulge and disk potential, NFW halo potential, and Long-Murali bar potential.

It can be noticed that the only difference between the two models is the bulge potential: due to the presence of the cut-off radius in Model II, the influence of bulge is confined to a smaller volume than in Model I.

The results of the *equipot()* function show that both models used in the current work are consistent with the theoretical mass distribution for each component, and therefore it is possible to proceed with the integration of the orbit of specific targets.

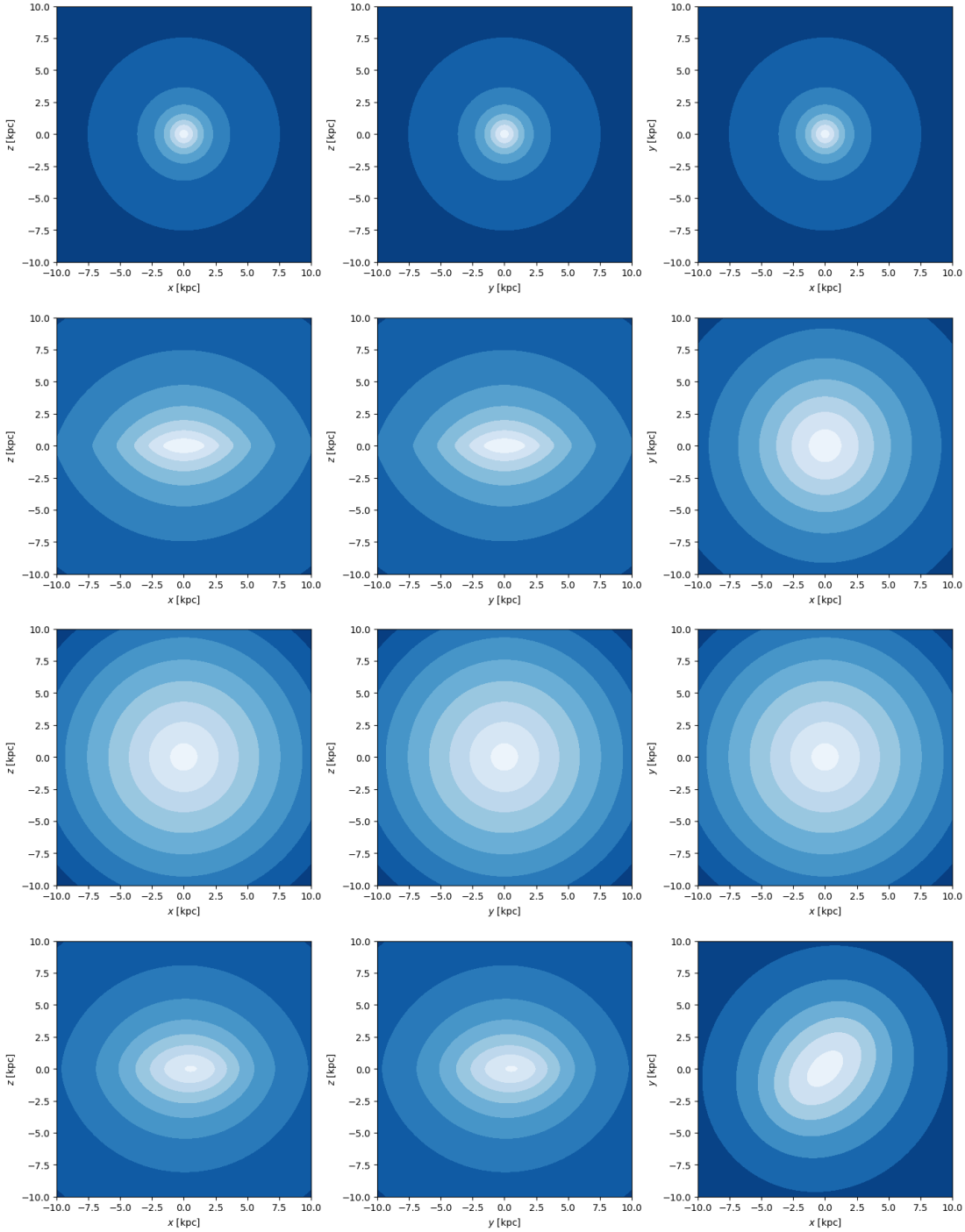

Figure 6.2: From top to bottom, bulge, disk, halo, and bar equipotential lines are presented using Model I.

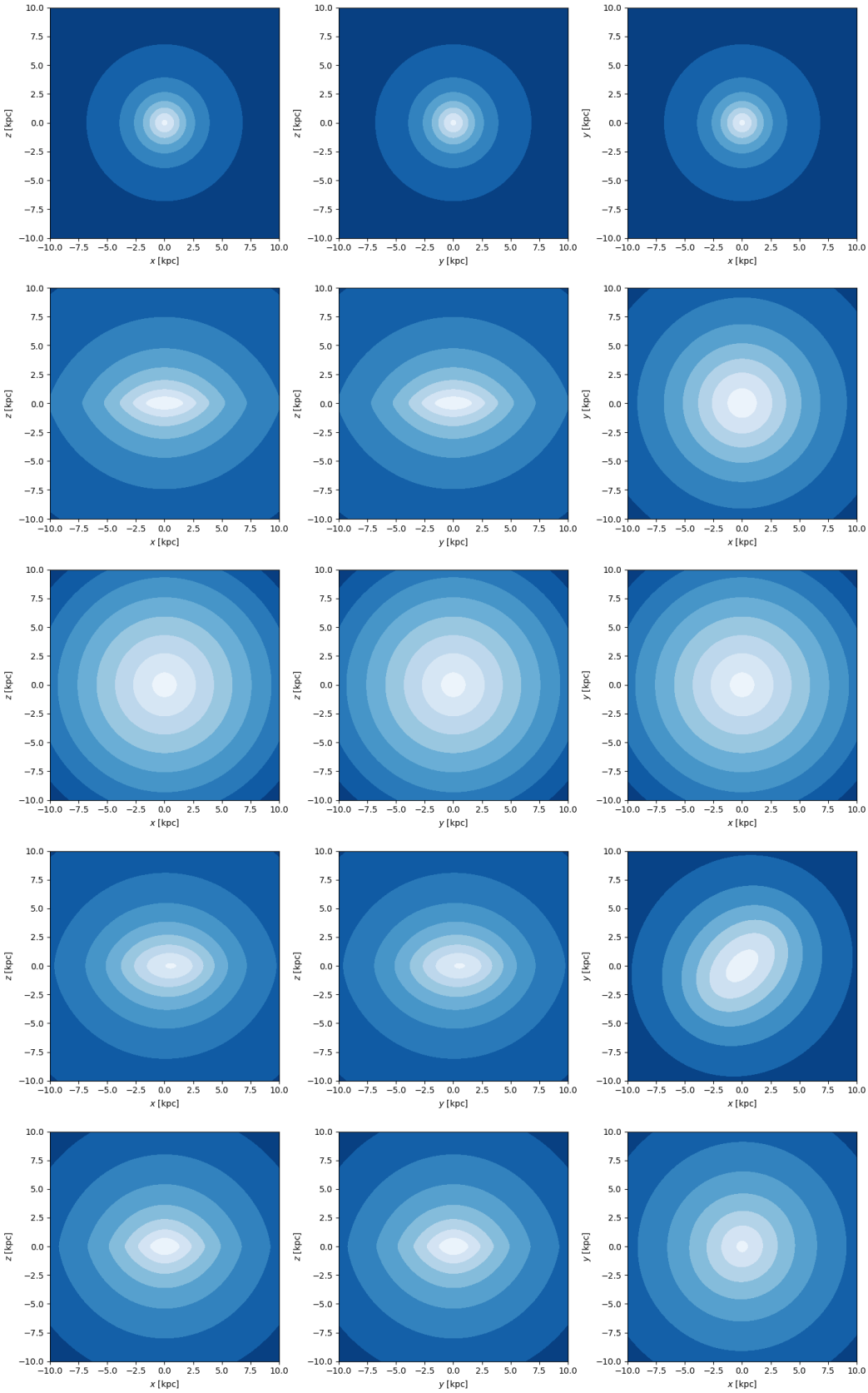

Figure 6.3: Equipotential lines using Model II, where (from top to bottom) bulge, disk, halo, and bar components are presented; the bottom row represents the total potential, where all the components are switched on at the same time.

6.2 Orbits integration

According to the code description in Chapter 5, it is possible to represent an integrated orbit with different views due to the WHVN algorithm. In the next figures, some results will be presented for three test objects: Palomar 1 from the general Gaia EDR3 dataset, IC 1257 from the GSE population, and NGC 288 from the Pontus population. The Palomar 1 cluster can be found in the halo of the Outer Arm of the Milky Way, as a Galactic intermediate-age globular cluster. According to [Van Den Bergh & Mackey, 2004], Palomar 1 has relatively high [Fe/H] abundances and a similar evolutionary history to Terzan 7: originally, they were both most likely dwarf spheroidal galaxies that were later destroyed by tidal forces. In Figure 6.4, the Palomar 1 orbits are represented in both models, with a bar potential.

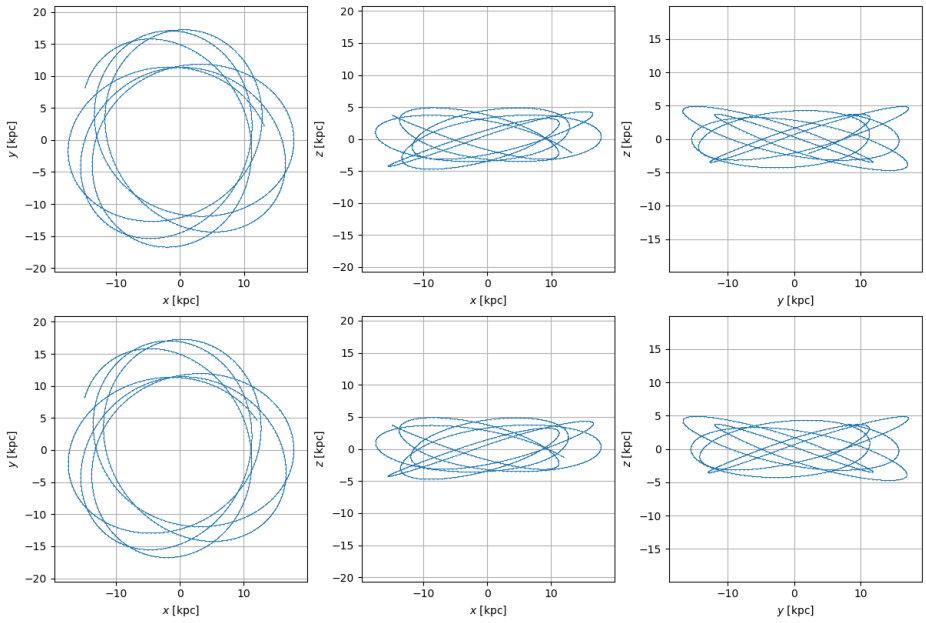

Figure 6.4: Palomar 1 orbits are represented with *orbits()* function, considering the bar, with Model I (up) and Model II (down). The differences between the two models for Palomar 1 orbits are very small. The integration time is 2 Gyr ($2{\cdot}10^4$ 0.1 Myr steps).

Even if its discovery occurred many years ago, the globular cluster IC 1257 still has attention if it is associated with merging events. According to [Harris et al. 1997], it is a compact star cluster situated close to the celestial equator (l=17°, b=+15°), highly reddened beyond the GC, positioned approximately 24 kpc from the Sun, and ∼16kpc beyond the Galactic center. Looking at its colour-magnitude diagram, IC 1257, it is possible to find similarities with the well-known M 13 globular cluster, with a relatively low metallicity [Fe/H] ≃-1.7. Thanks to WHVN's function *orbits()*, it is possible to take a closer look at IC 1257 orbit in Figure 6.5, using Model II with and without bar.

Following [Gontcharov et al. 2021] work on the Galactic globular cluster, most of the highly populated globular clusters around the Milky Way have high-density cores. On the other hand, NGC 288 represents one of the low-concentration clusters, with stars loosely bound together. It is located approximately 8.96kpc away from Earth, positioned in the constellation Sculptor, and has an estimated age of 10.6 Gyr. Observations show that NGC 288 has a very large and dense core with a diffuse, irregular ring. In Figure 6.6, the orbit of NGC 288 can be found in two Milky Way configurations: in the first image, the presence of a rotating bar is neglected, while in the second image, the bar component is switched on.

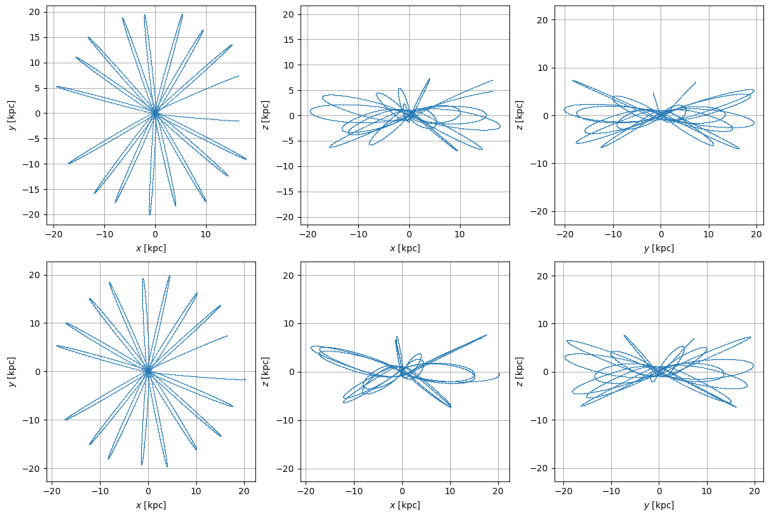

Figure 6.5: The orbits over 2D planes are represented for IC 1257 with Model II: bar potential is not considered in the upper image, while in the lower one bar influence can be seen from central regions within 10 kpc. The integration time used is 3.5 Gyr ($3.5{\cdot}10^4$ steps of 0.1 Myr).

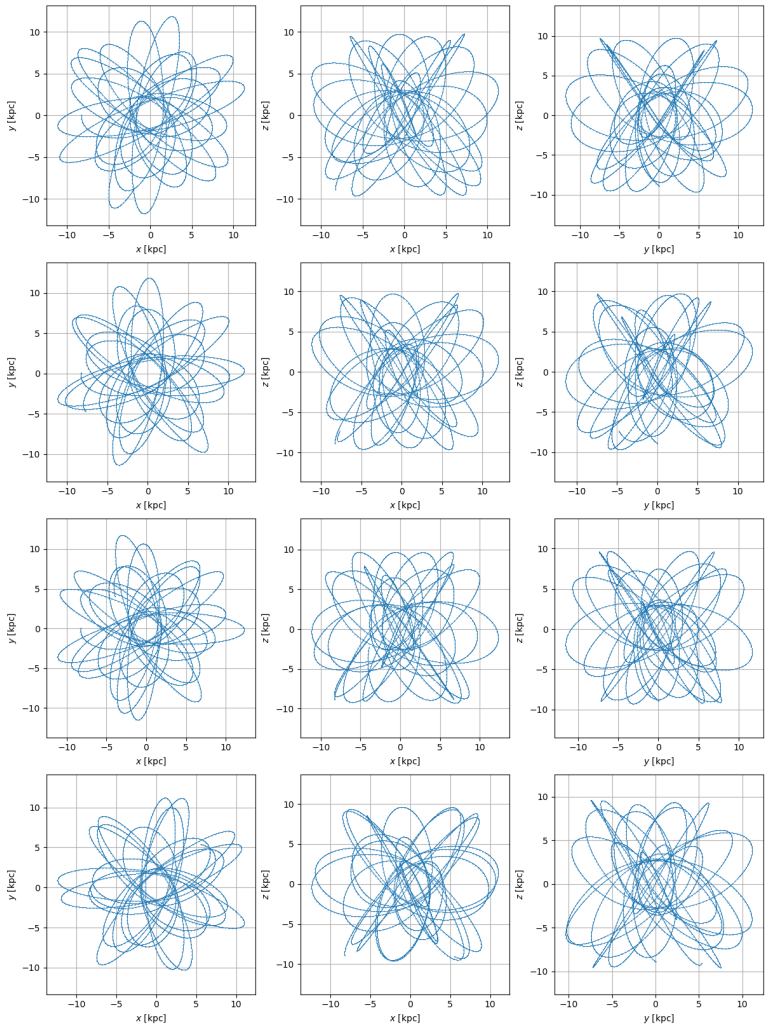

Figure 6.6: Orbits projection for NGC 288 in all configurations: the first two rows represent Model I and Model II without bar influence, while the lower ones show the same models with bar potential. The integration time used is 4 Gyr ($4{\cdot}10^4$ steps of 0.1 Myr).

Other useful views of the previous objects are represented in Figures 6.7 and 6.8 by the functions *mer_plane()* and *orbit3D()*. These functions can shed more light on particular differences introduced by the bar presence or by the used model itself. Nonetheless, the consequences of bar presence and the choice of the model are very small.

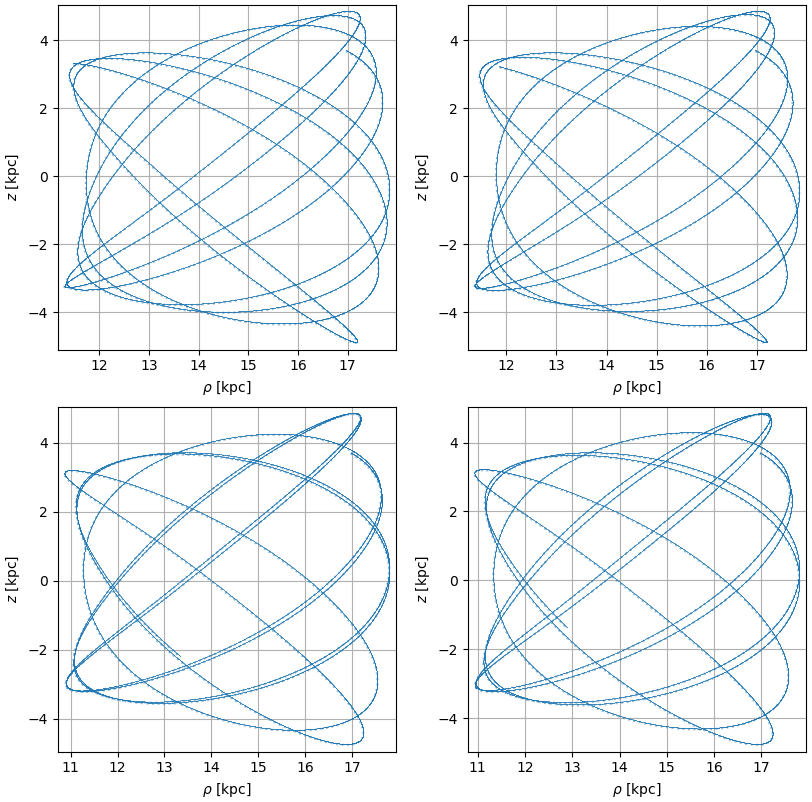

Figure 6.7: The meridional planes for Palomar 1 in all configurations: the first two rows represent Model I and Model II without bar influence, while the lower ones show the same models with bar potential. The integration time is 2 Gyr ($2{\cdot}10^4$ steps of 0.1 Myr)

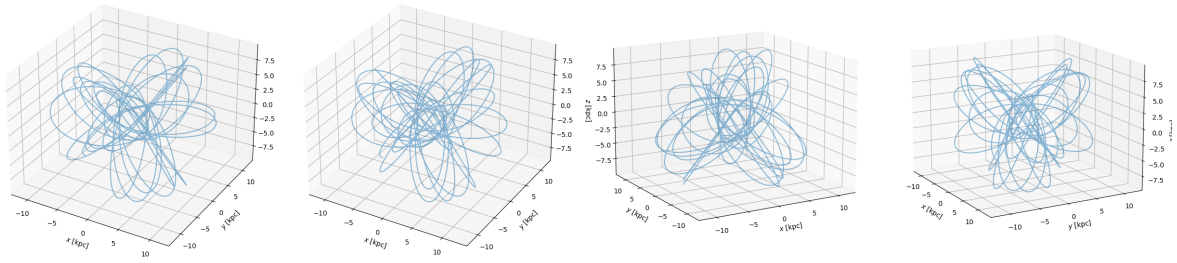

Figure 6.8: Three-dimensional scatter plot for NGC 288 with Model I, with (second and fourth images) and without (first and third images) bar potential, in different orientations. These plots can be useful to verify orbital differences using an interactive plot that can be rotated by the user. The integration time used is 4 Gyr ($4{\cdot}10^4$ steps of 0.1 Myr).

6.3 Angular momentum and total energy

One of the most interesting indicators in the following study is represented by the variation in time of the angular momentum along the z-axis and the total energy. Recalling what is written in Chapter 2, the presence of the bar breaks the constant values of L_z and E and makes them vary (or oscillate). As can be seen in Figure 6.9, 47 Tucanae (also called NGC 104) experienced this discrepancy between the two configurations. The integration time of 1 Gyr was chosen to highlight where small variations in L_z and E occur during the orbit, while error propagation with the Monte Carlo method is based on a normal distribution in Figure 6.10.

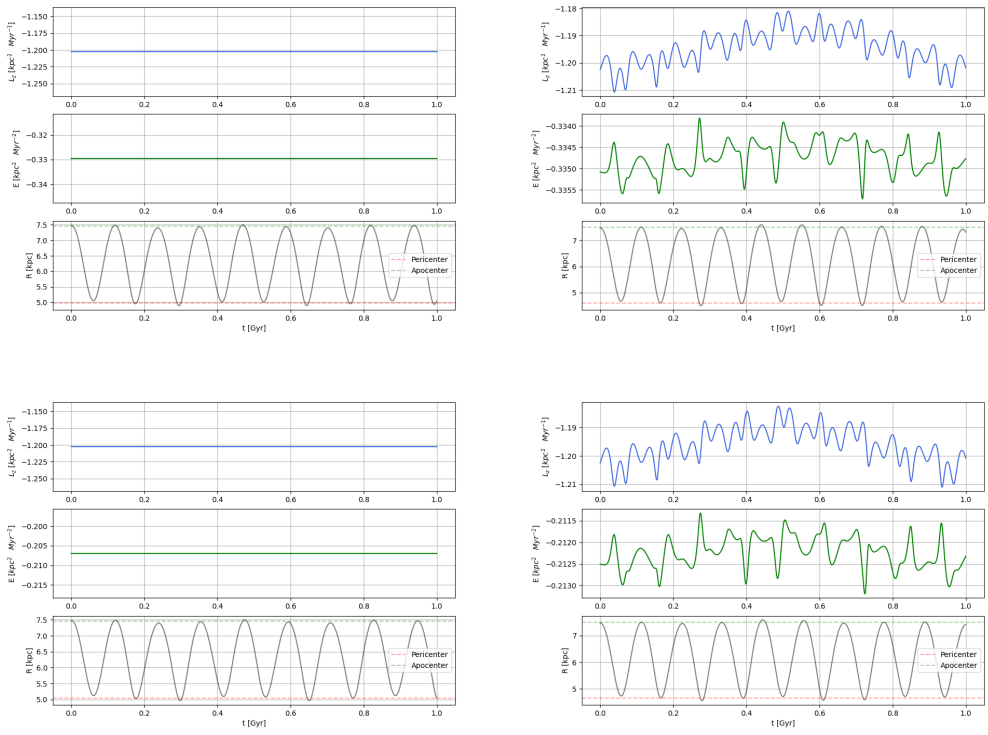

Figure 6.9: Angular momentum L_z and total energy E variation over integration time, compared with the variation of distance between apocenter and pericenter, for 47 Tucanae for Model I (upper figure) and Model II (lower figure), while figures on the left show resulting L_z and E calculation with bar. The integration time is 1 Gyr (10^4 steps of 0.1 Myr).

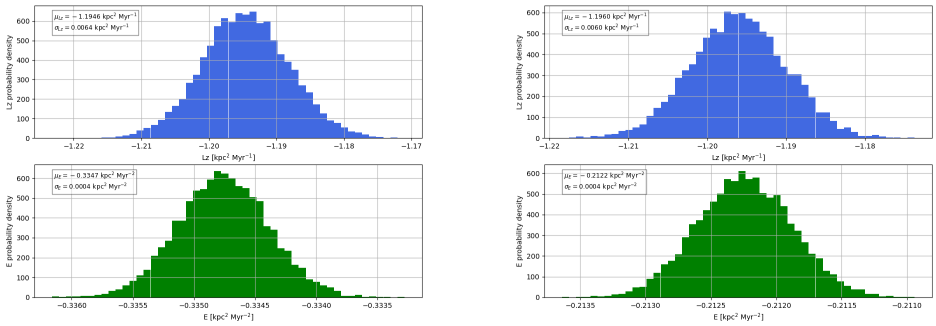

Figure 6.10: The Monte Carlo propagation of error for angular momentum L_z and total energy E variation over integration time for 47 Tucanae is shown for Model I (left figure) and Model II (right figure). The integration time is 1 Gyr (10^4 steps of 0.1 Myr).

Furthermore, a 5 Gyr orbit is integrated for both models in Figure 6.11.

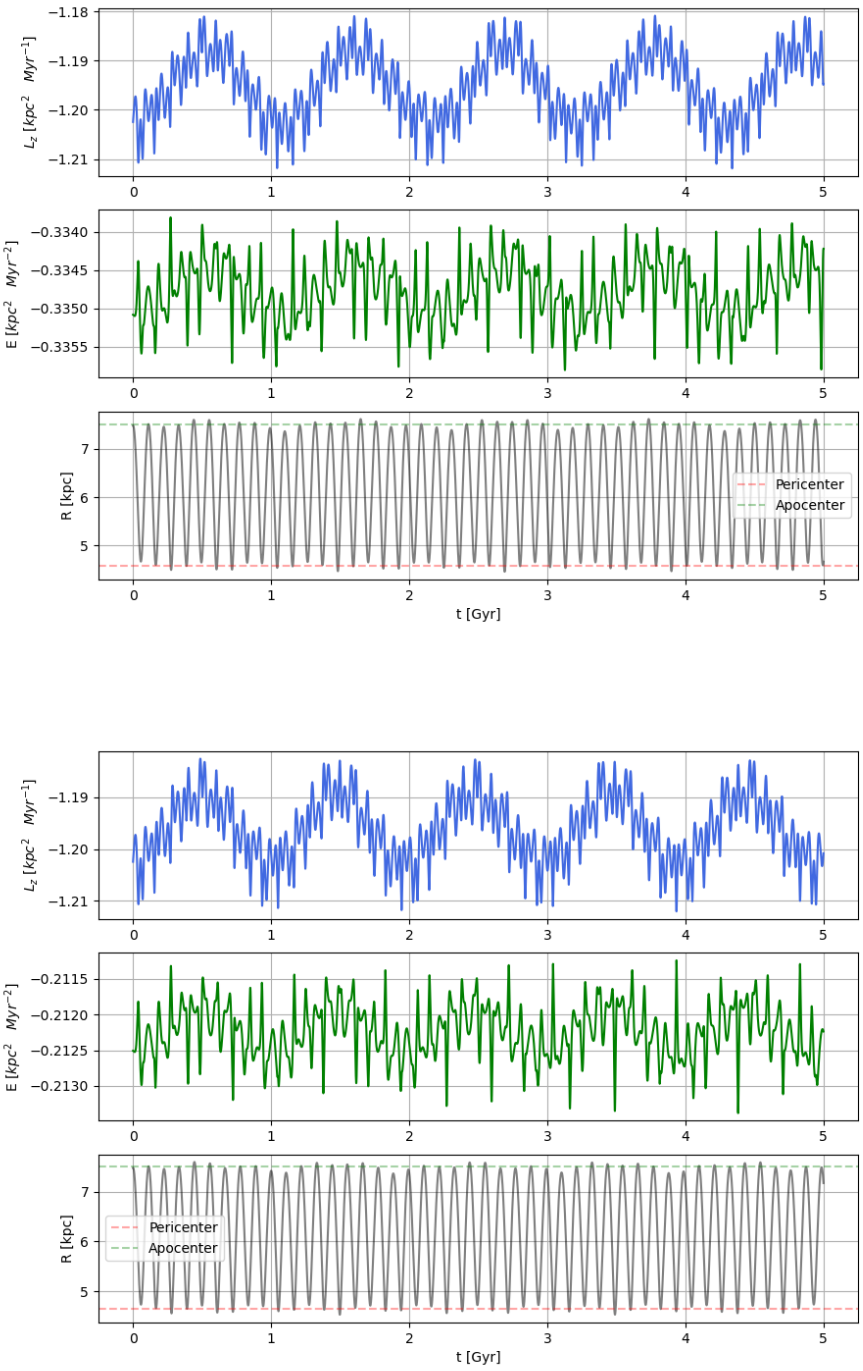

Figure 6.11: Same configuration of Figure 6.9 with only bar components for Model I (upper image) and Model II (lower image), with 5 Gyr of integration time ($5{\cdot}10^4$ steps of 0.1 Myr).

Another method for error propagation consists of integrating many orbits at the same time and applying a Gaussian scatter to initial positions and velocities, where the value of the scatter is set in accordance with Gaia EDR3 errors on initial data. The integration of 25 and 50 orbits with bar potential can be found in Figure 6.12, using Model II as an example.

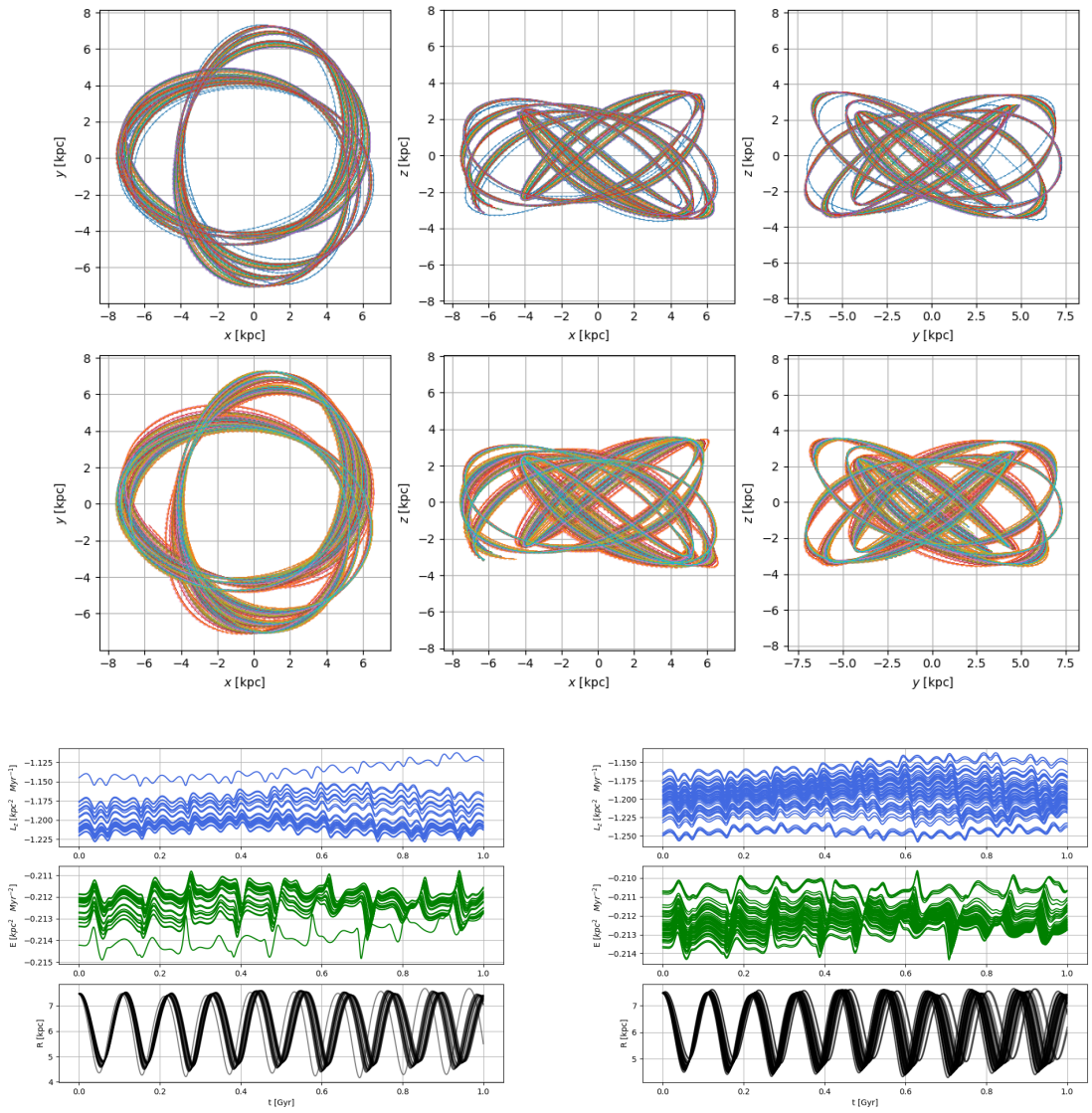

Figure 6.12: Upper images represent 25 and 50 orbits integrated from 47 Tucanae with Model II with bar, while lower ones show L_z and E variation in time, with 1 Gyr of integration time ($1{\cdot}10^4$ steps of 0.1 Myr).

6.4 Population analysis

As described in Chapter 5, the *compare_pop()* the function provided in WHVN is fundamental to verify which globular cluster belongs to a specific merging event. For this specific purpose, it should be noted that, to obtain proper eccentricities, the target's orbit should be a close orbit, and so higher integration times are required. Moreover, not all targets are available due to the lack of data described in Chapter 3 (nine objects have missing data): anyway, analysing 161 globular clusters at the same time requires a lot of computational time.

In the following framework, the available population is presented: globular clusters of Gaia EDR3 that do not belong to GSE or Pontus are displayed as grey dots; candidates for GSE are shown as blue dots and Pontus candidates as green ones; the tentative associations NGC 7089/M 2 and NGC 6864/M 75 are represented in black and purple. In Figures 6.13 and 6.14, an overview of the whole population is presented for Model I and Model II, with axis-symmetric and non axis-symmetric potentials.

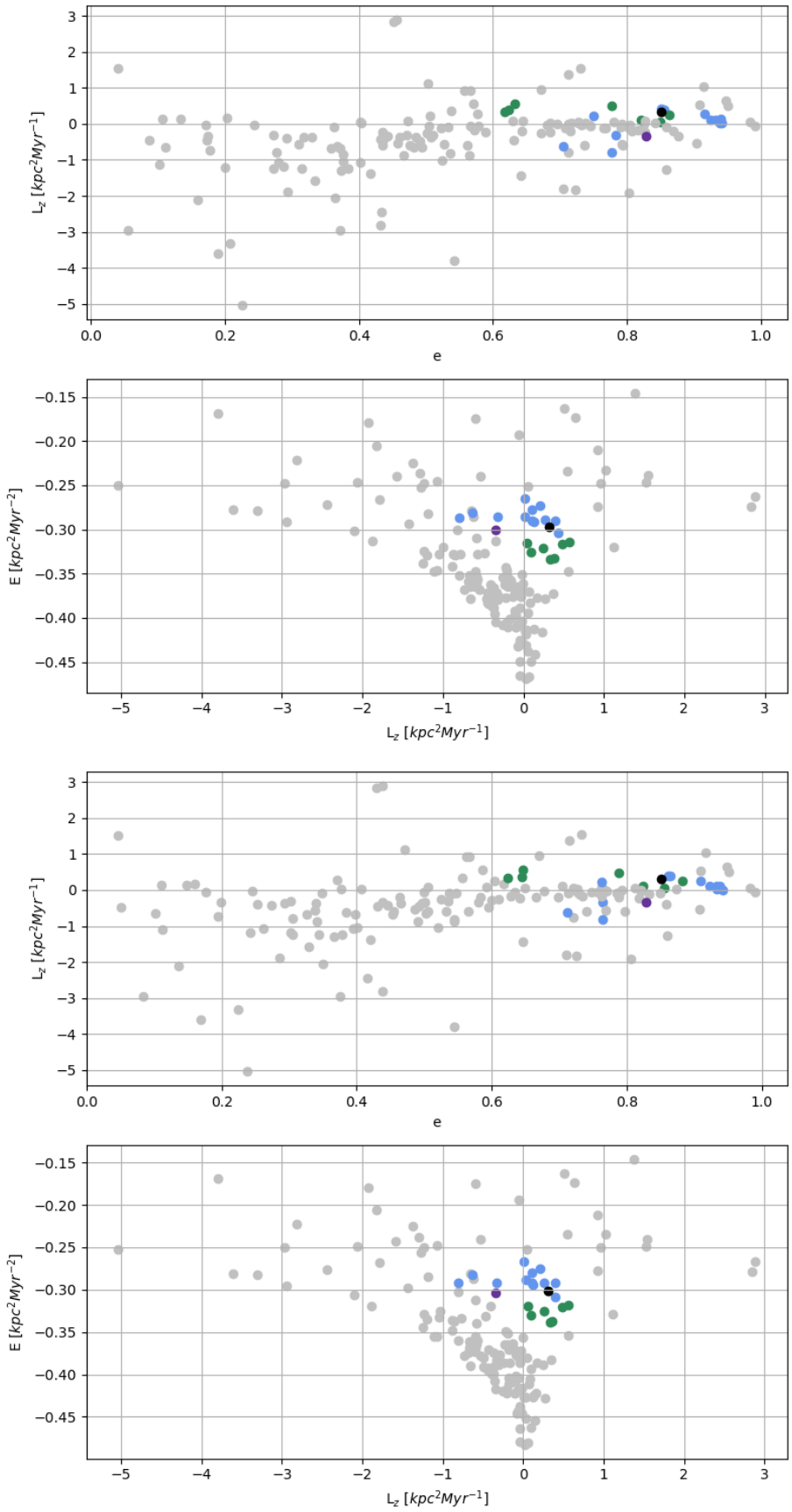

Figure 6.13: Model I population comparison: the first two panels show eccentricity e vs. L_z and L_z vs. total energy E of the entire population in the Milky Way potential with bulge, disk, and halo; the lower panels include bar contribution. Integration time was set to 2 Gyr with $2{\cdot}10^4$ steps of 0.1 Myr.

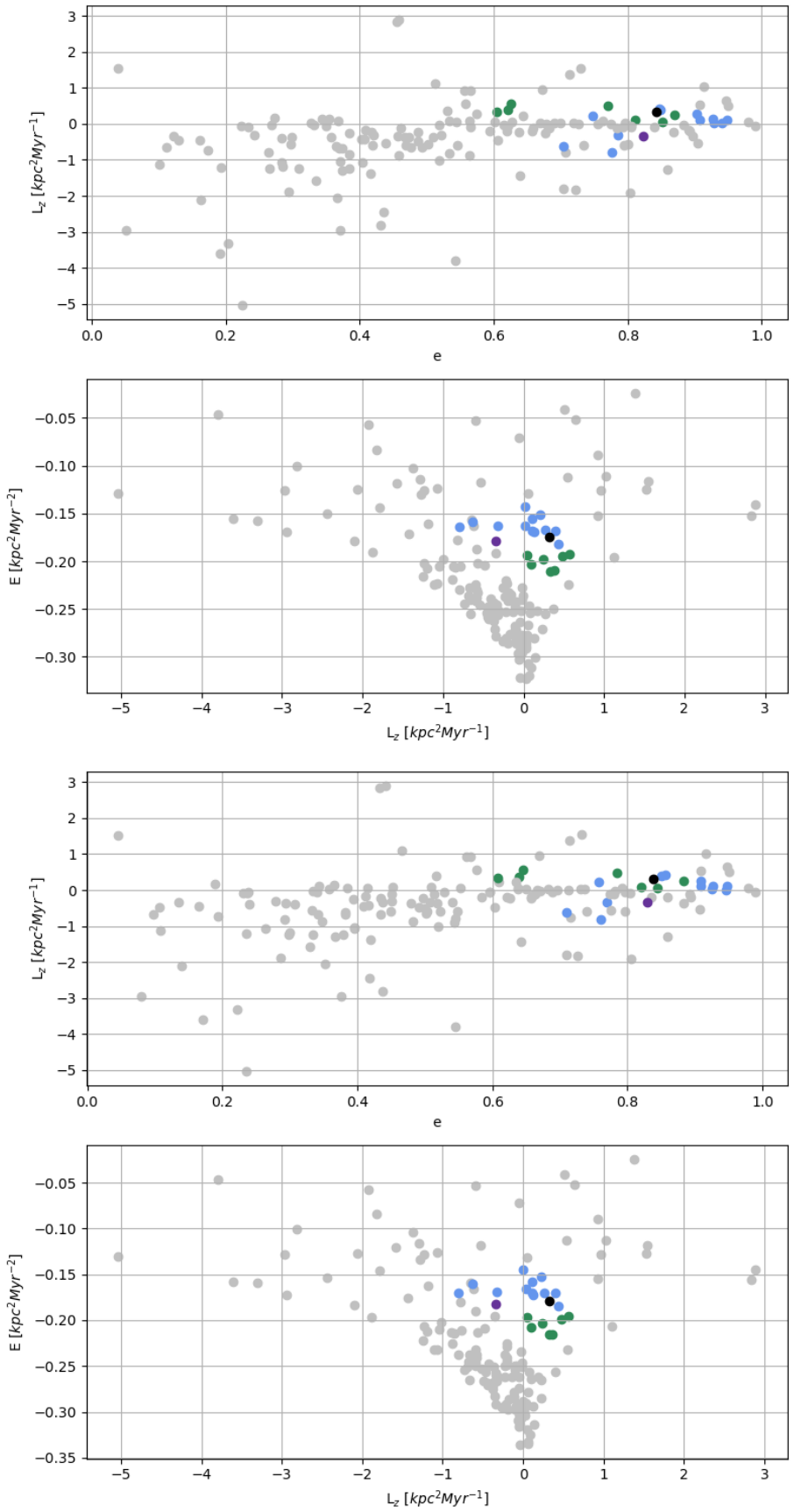

Figure 6.14: The same plots and parameters as in Figure 6.13 for a 2 Gyr orbit ($2 \cdot 10^4$ steps of 0.1 Myr), integrated with Model II.

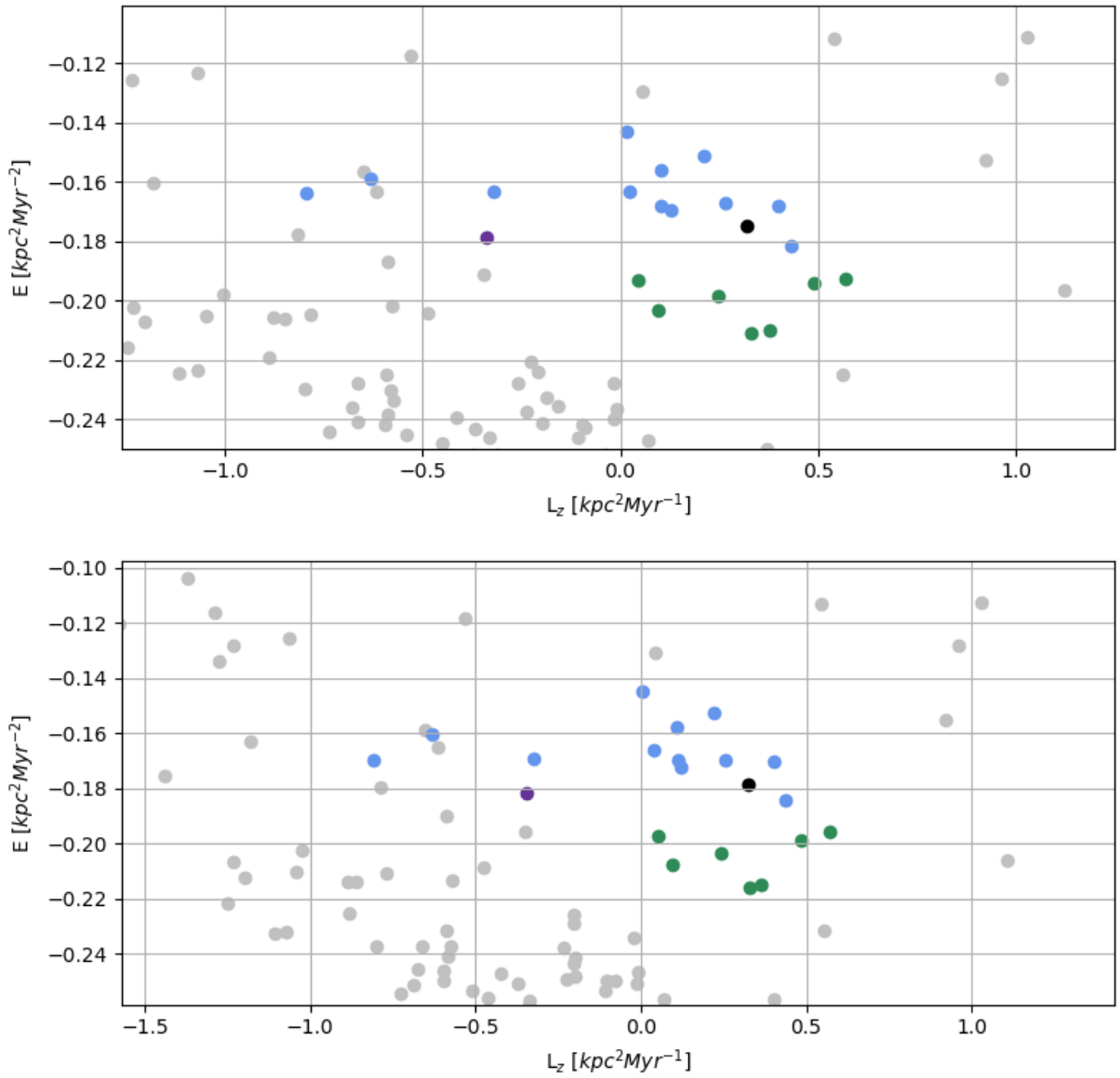

Figure 6.15: It is possible to recognise all 12 verified members of GSE (blue), 7 verified members of Pontus (green), and the two tentative candidates, NGC 7089/M 2 (black) and NGC 6864/M 75 (purple) in the target populations computed in Figure 6.14. As seen in both plots, GSE members typically have more energy than Pontus members, and L_z values can span a wider range than Pontus; thus, NGC 7089/M 2 and NGC 6864/M 75 (purple) appear to be much closer to GSE than Pontus. In any case, the display of GSE and Pontus members in the L_z vs. E plot is consistent with [Naidu et al. 2020], [Malhan et al. 2022], and [Malhan, 2022].

Chapter 7

Conclusions

During most of the orbit integrations and calculations of the various orbital parameters discussed in the current work, it is possible to notice how the two models differ in computational time: Model I, which is constructed with custom potentials, is slower than Model II, which is constructed with only GALA built-in potentials. This is probably connected to the structure of the GALA package that returns the best results in the shortest time possible; using a custom potential implies that the programme needs to accept a new component, control it, insert it inside the calculation, and use it whenever it is called, and this requires a much higher computational time.

For example, the integration performed for figures 6.13 and 6.14 took approximately 2 hours for Model I and 40 minutes for Model II, due to the high number of targets and high integration time for each target.

Other interesting implications can be made regarding L_z and E. As seen before in Chapter 2, L_z and E should be constant in axis-symmetric potential, while they should vary with non axis-symmetric components (such as the bar potential). This was confirmed for both Model I and Model II, but the degree of variation is extremely small compared to the average value for L_z and E: errors are negligible from two different uncertainty approaches.

As a result, in the first approximation, it is acceptable to treat L_z and E as constants while keeping in mind that error propagation should be performed in all cases. It is also possible that particular targets have extreme initial values, and so L_z and E could show a higher degree of variation for reference values.

Then, population analysis showed two fundamental results, confirmed by both models, with and without bar: as discussed by [Malhan et al. 2022], the Pontus and Gaia-Sausage/Enceladus members displayed similar values with high eccentricity and low angular momentum, so it is ideally impossible to separate completely these populations with only those values.

The comparison between angular momentum L_z and total energy E gives a better separation between the two events, where the Pontus members have higher energies than the Gaia-Sausage/Enceladus population. This result allows for a better separation between the two events, where the Gaia-Sausage/Enceladus members have lower energies than the Pontus population. So, it is possible to assume that the two tentative members, NGC 7089/M 2 and NGC 6864 / M 75 seem more connected to the GSE population than Pontus.

The WHVN algorithm appears to be a reliable orbital calculation tool that can be easily

implemented with more precise potentials. Also, with future data releases, it represents a simple code that converts celestial coordinates, proper motions, and velocities along the line of sight into galactocentric coordinates and then orbits.

Ideally, the WHVN algorithm could also be associated with different kinds of targets, with proper potential and framework choices, like a planet and its satellites, a black hole and its companion or the cluster center, and unresolved binaries.

Regarding WHVN results on merging events, a much deeper study needs to be done considering other non-orbital parameters like metallicity variation, isochrones, and evolutionary studies on each star in the cluster population.

Bibliography

[Allen & Santillan, 1991] - C. Allen and A. Santillan. "An improved model of the galactic mass distribution for orbit computations.". Revista Mexicana de Astronomia y Astrofisica, Vol. 22, p. 255. 1991.

[Allen & Martos, 1986] - C. Allen and M.A. Martos. "A simple, realistic model of the galactic mass distribution for orbitcomputations.". Revista Mexicana de Astronomia y Astrofisica, Vol. 13, p. 137-147, 1986.

[Athanassoula, 2005] - Athanassoula, E. "On the nature of bulges in general and of box/-peanut bulges in particular: input from N-body simulations ". Monthly Notices of the Royal Astronomical Society, Volume 358, Issue 4, pp. 1477-1488, 2005.

[Bajkova et al. 2020] - A. T. Bajkova, G. Carraro, V. I Korchagin, N. O. Budanova, and V. V. Bobylev. "Milky Way Subsystems from Globular Cluster Kinematics Using Gaia DR2 and HST Data". The Astrophysical Journal, Volume 895, Number 1, May 2020.

[Bajkova & Bobylev, 2017] - A. T. Bajkova and V. V. Bobylev. "Refinement of Parameters of Six Selected Galactic Potential Models". Open Astron., Volume 26, Issue 1, pp. 72-79, 2017.

[Bajkova & Bobylev, 2016] - A. T. Bajkova and V. V. Bobylev. "Rotation Curve and Mass Distribution in the Galaxy from the Velocities of Objects at Distances up to 200 kpc". Astronomy Letters, Vol. 42, No. 9, pp. 567-582, 2016

[Baumgardt & Vasiliev, 2021] - H. Baumgardt and E. Vasiliev. "Accurate distances to Galactic globular clusters through a combination of Gaia EDR3, HST and literature data". 2021.

[Belokurov et al. 2018] - V. Belokurov, D. Erkal, N. W. Evans, S. E. Koposov and A. J. Deason. "Co-formation of the disc and the stellar halo". Monthly Notices of the Royal Astronomical Society, Volume 478, Issue 1, pp. 611–619, 2018.

[Binney & Tremaine, 2008] - J. Binney and S. Tremaine. "Galactic Dynamics: Second Edition". Published by Princeton University Press, Princeton, NJ USA. 2008.

[Binney et al. 1991] - J. Binney, ; O.E. Gerhard, A.A. Stark, J. Bally, K.I. Uchida. "Understanding the kinematics of Galactic Centre gas.". Monthly Notices of the Royal Astronomical Society, Vol. 252, 210, 1991.

[Bland-Hawthorn & Gerhard, 2016] - J. Bland-Hawthorn and O. Gerhard. "The Galaxy in Context: Structural, Kinematic, and Integrated Properties". Annual Review of Astronomy and Astrophysics, vol. 54, p.529-596. 2016.

[Blitz & Spergel, 1991] - L.Blitz and D.N.Spergel. "Direct Evidence for a Bar at the Galactic Center". Astrophysical Journal v.379, p.631, 1991.

[Bovy, 2015] - J. Bovy. "galpy: A python library for galactic dynamics". The Astrophysical Journal Supplement Series, Volume 216, Issue 2, article id. 29, 27 pp., 2015.

[Cole et al. 2010] - N. Cole, T. Desell, D. Lombraña González, F. Fernández de Vega, M. Magdon-Ismail, H. Newberg, B. Szymanski, and C. Varela . "Evolutionary Algorithms on Volunteer Computing Platforms: The MilkyWay@Home Project". Studies in Computational Intelligence, vol 269. Springer, Berlin, Heidelberg, 2010.

[Di Matteo et al. 2019] - P. Di Matteo, M. Haywood, M. D. Lehnert, D. Katz, S. Khoperskov, O.N. Snaith, A. Gómez, and N. Robichon. "The Milky Way has no in-situ halo other than the heated thick disc". A&A, Volume 632, December 2019.

[Drimmel & Poggio, 2018] - R. Drimmel and E. Poggio. "On the Solar Velocity". Research Notes of the AAS, Volume 2, Number 4, 2018.

[Fu-Chi Yeh et al. 2020] - F.C Yeh, G Carraro, V. I. Korchagin, C. Pianta, and S. Ortolani. "The origin of globular cluster FSR 1758". A&A, Volume 635, March 2020.

[Gaia Collaboration, 2020] - Gaia Collaboration . "Gaia Data Release 2: Kinematics of globular clusters and dwarf galaxies around the Milky Way". A&A Gaia DR2 Special Issue, 2020.

[Gaia Collaboration et al. 2020] - Gaia Collaboration. "Gaia Early Data Release 3. Summary of the contents and survey properties". Astronomy & Astrophysics, Volume 649, id.A1, 20 pp, 2020.

[Gilmore, 1996] - G. Gilmore. "Early and Late Evolution of the Milky Way". Formation of the Galactic Halo, Inside and Out, ASP Conference Series, Vol. 92, Heather Morrison and Ata Sarajedini, eds., p. 161, 1996.

[Gilmore & Feltzing, 1999] - G. Gilmore and S.Feltzing. "Dynamical Evolution of the Galaxy". The Evolution of Galaxies on Cosmological Timescales, ASP Conference Series,Vol. 187. Edited by J. E. Beckman and T. J. Mahoney, ISBN: 1-58381-013-7,p.20-30, 1999.

[Gontcharov et al. 2021] - G.A. Gontcharov, M.Y. Khovritchev, A. V. Mosenkov, V.B. Il'in, A.A. Marchuk, S.S. Savchenko, A.A. Smirnov, P.A. Usachev, and D.M. Poliakov. "Isochrone fitting of Galactic globular clusters – III. NGC 288, NGC 362, and NGC 6218 (M12) ". Monthly Notices of the Royal Astronomical Society, Volume 508, Issue 2, Pages 2688–2705, 2021.

[Grand et al. 2020] - R.J.J. Grand, D. Kawata, V. Belokurov, A. J. Deason, A. Fattahi, F. Fragkoudi, F.A. Gómez, F. Marinacci, and R. Pakmor. "Sausage & Mash: The dual origin of the Galactic thick disc and halo from the gas-rich Gaia-Enceladus-Sausage merger". MNRAS accepted, 2020.

[Harris, 2010] - W. E. Harris. "A New Catalog of Globular Clusters in the Milky Way". 2010.

[Harris et al. 1997] - W.E. Harris, R.L. Phelps, B.F. Madore, O. Pevunova,; B.A. Skiff, C. Crute, B. Wilson, and B.A. Archinal. "IC 1257:A New Globular Cluster in the Galactic Halo". Astronomical Journal v.113, p. 688-691, 1997.

[Haywood et al. 2018] - M. Haywood , P. Di Matteo , M. D. Lehnert, O. Snaith, S. Khoperskov and A. Gómez. "In Disguise or Out of Reach: First Clues about In Situ and Accreted Stars in the Stellar Halo of the Milky Way from Gaia DR2". The Astrophysical Journal, Volume 863, Issue 2, article id. 113, 10 pp., 2018.

[Helmi et al. 2018] - A. Helmi, C. Babusiaux, H. H. Koppelman, D. Massari, J. Veljanoski and A. G.A. Brown. "The merger that led to the formation of the Milky Way's inner stellar halo and thick disk". Nature, issue of Nov. 1st, 2018.

[Hernquist, 1990] - L. Hernquist. "An Analytical Model for Spherical Galaxies and Bulges ". Astrophysical Journal v.356, p.359, 1990.

[Horta et al. 2022] - D. Horta, R.P. Schiavon, J.T. Mackereth, D.H. Weinberg, S. Hasselquist, D. Feuillet, R.W. O'Connell, B. Anguiano, C. Allende-Prieto, R.L. Beaton, D. Bizyaev, K. Cunha, D. Geisler, D.A. García-Hernández, J. Holtzman, H. Jönsson, R.R. Lane, S.R. Majewski, S. Mészáros, D. Minniti, C. Nitschelm, M. Shetrone, V.V. Smith, and G. Zasowski. "The chemical characterisation of halo substructure in the Milky Way based on APOGEE". eprint arXiv:2204.04233, 2022.

[Ibata et al. 1994] - R. A. Ibata, G. Gilmore, and M. J. Irwin . "A dwarf satellite galaxy in Sagittarius". Nature, Volume 370, Issue 6486, pp. 194-196, 1994.

[Irrang et al. 2013] - A. Irrgang, B. Wilcox, E. Tucker and L. Schiefelbein. "Milky Way mass models for orbit calculations". A&A, Volume 549, January 2013.

[Jílková et al. 2012] - L. Jílková, G. Carraro, B. Jungwiert, and I. Minchev. "The origin and orbit of the old, metal-rich, open cluster NGC 6791". A&A, Volume 541, May 2012.

[Johnson & Soderblom, 1987] - D.R.H Johnson and D.R. Soderblom. "Calculating Galactic Space Velocities and Their Uncertainties, with an Application to the Ursa Major Group". Astronomical Journal v.93, p.864, 1987.

[Karam & Sills, 2022] - J. Karam, and A. Sills. "Modelling star cluster formation: mergers". Monthly Notices of the Royal Astronomical Society, Volume 513, Issue 4, pp.6095-6104, 2022.

[Kim et al. 2021] - Y.K. Kim, Y.S. Lee, T.C. Beers, and J.R. Koo. "Evidence for Multiple Accretion Events in the Gaia-Sausage/Enceladus Structures". The Astrophysical Journal Letters, Volume 911, Number 2, 2021.

[Koppelman et al. 2018] - H.H. Koppelman, A. Helmi, D. Massari, A.M. Price-Whelan, and T.K. Starkenburg. "Multiple retrograde substructures in the Galactic halo: A shattered view of Galactic history". A&A, Volume 631, 2019.

[Lacey & Cole, 1993] - C. Lacey and S.Cole. "Merger rates in hierarchical models of galaxy formation". Monthly Notices of the Royal Astronomical Society (ISSN 0035-8711), vol. 262, no. 3, p. 627-649, 1993.

[Lancaster et al. 2019] - L. Lancaster, S.E. Koposov, V. Belokurov, N. Wyn Evans and A. J. Deason. "The halo's ancient metal-rich progenitor revealed with BHB stars". Monthly notices of the Royal Astronomical Society., 486 (1). pp. 378-389, 2019.

[Long & Murali, 1992] - K. Long and C. Murali. "Analytical Potentials for Barred Galaxies". Astrophysical Journal v.397, p.44, 1992.

[Mackereth et al. 2019] - J. T. Mackereth, R. P. Schiavon, J. Pfeffer , C.R. Hayes, J. Bovy, B. Anguiano, C.A. Prieto, S. Hasselquist, J. Holtzman, J.A. Johnson, S. R. Majewski, R. O'Connell, M. Shetrone, P. B. Tissera and J. G. Fernandez-Trincado. "The origin of accreted stellar halo populations in the Milky Way using APOGEE, Gaia, and the EAGLE simulations". Monthly Notices of the Royal Astronomical Society, Volume 482, Issue 3, pp. 3426-3442, 2019.

[Malhan et al. 2022] - K. Malhan, R. A. Ibata, S. Sharma, B. Famaey, M. Bellazzini, R. G. Carlberg, R. D'Souza, Z. Yuan, N. F. Martin, and G.F. Thomas. "The Global Dynamical Atlas of the Milky Way Mergers: Constraints from Gaia EDR3–based Orbits of Globular Clusters, Stellar Streams, and Satellite Galaxies". The Astrophysical Journal, Volume 926, Number 2, 2022.

[Malhan, 2022] - K. Malhan. "A new member of the Milky Way's family tree: Characterizing the Pontus merger of our Galaxy". Draft version April 21, 2022.

[McMillan, 2017] - P. J. McMillan. "The mass distribution and gravitational potential of the Milky Way". Monthly Notices of the Royal Astronomical Society, Volume 465, Issue 1, Pages 76–94, February 2017.

[Minniti et al. 2021] - D. Minniti, V. Ripepi, J.G. Fernández-Trincado, J. Alonso-García, L.C. Smith, P.W. Lucas, M. Gómez, J.B. Pullen, E.R. Garro, F. Vivanco Cádiz, M. Hempel, M. Rejkuba, R.K. Saito, T. Palma, J.J. Clariá, M. Gregg, and D. Majaess. "Discovery of new globular clusters in the Sagittarius dwarf galaxy". A&A, Volume 647, 2021.

[Miyamoto & Nagai, 1975] - M. Miyamoto and R. Nagai. "Three-dimensional models for the distribution of mass in galaxies.". Publications of the Astronomical Society of Japan, Vol. 27, 533-543, 1975.

[Myeong et al. 2018] - G.C. Myeong , N.W. Evans, V. Belokurov, J.L. Sanders, and S.E. Koposov. "The Sausage Globular Clusters". The Astrophysical Journal Letters, Volume 863, Issue 2, article id. L28, 5 pp., 2018.

[Naidu et al. 2020] - R. P. Naidu, C. Conroy, A. Bonaca, B. D. Johnson, Y.S. Ting, N. Caldwell, D. Zaritsky, and P. A. Cargile. "Evidence from the H3 Survey That the Stellar Halo Is Entirely Comprised of Substructure". The Astrophysical Journal, Volume 901, Number 1, 2020.

[Navarro et al. 1996] - J.F. Navarro, C.S. Frenk, and S.D.M. White. "The Structure of Cold Dark Matter Halos". Astrophysical Journal v.462, p.563, 1996.

[Navarro et al. 1997] - J.F. Navarro, C.S. Frenk, and S.D.M. White. "A Universal Density Profile from Hierarchical Clustering". The Astrophysical Journal, Volume 490, Issue 2, pp. 493-508, 1997.

[Palous et al. 1993] - J. Palous, B. Jungwiert, and J. Kopecky. "Formation of rings in weak bars: inelastic collisions and star formation.". Astronomy and Astrophysics, Vol. 274, p. 189-202, 1993.

[Pichardo et al. 2004] - B. Pichardo, M. Martos, and E. Moreno. "Models for the Gravitational Field of the Galactic Bar. An Application to Stellar Orbits in the Galactic Plane and Orbits of Some Globular Clusters". Astrophys. J. 609, 144-165, 2004.

[Price-Whelan et al. 2017] - Adrian M. Price-Whelan. "Gala: A Python package for galactic dynamics". Journal of Open Source Software, 2(18), 388, 2017.

[Price-Whelan & Astropy Collaboration, 2018] - Adrian M. Price-Whelan and The Astropy Collaboration. "The Astropy Project: Building an Open-science Project and Status of the v2.0 Core Package". The Astronomical Journal, Volume 156, Number 3, 2018.

[Sanders et al. 2019] - J. L. Sanders , L. Smith, N. Wyn Evans, and P. Lucas. "Transverse kinematics of the Galactic bar-bulge from VVV and Gaia". Monthly Notices of the Royal Astronomical Society, Volume 487, Issue 4, Pages 5188–5208, August 2019.

[Shen et al. 2022] - J. Shen, G.M. Eadie, N. Murray, D. Zaritsky, J.S. Speagle, Y.S. Ting, C. Conroy, P.A. Cargile, B.D. Johnson, R.P. Naidu. "The Mass of the Milky Way from the H3 Survey". The Astrophysical Journal, Volume 925, Number 1, 2022.

[Sohn et al. 2018] - S.T. Sohn, L.L. Watkins, M. A. Fardal, R. P. Van Der Marel, A. J. Deason, G. Besla, and A. Bellini. "Absolute Hubble Space Telescope Proper Motion (HSTPROMO) of Distant Milky Way Globular Clusters: Galactocentric Space Velocities and the Milky Way Mass". The Astrophysical Journal, Volume 862, Number 1, 2018.

[Sormani et al. 2022] - M.C. Sormani, O.Gerhard, M. Portail, E. Vasiliev, J. Clarke. "The stellar mass distribution of the Milky Way's bar: an analytical model". Monthly Notices of the Royal Astronomical Society: Letters, Volume 514, Issue 1, pp.L1-L5, 2022.

[Van Den Bergh & Mackey, 2004] - S. Van Den Bergh and A.D. Mackey. "Globular clusters and the formation of the outer Galactic halo". Monthly Notices of the Royal Astronomical Society, Volume 354, Issue 3, Pages 713–719, 2004.

[Vasiliev & Baumgardt, 2021] - E. Vasiliev and H. Baumgardt. "Gaia EDR3 view on Galactic globular clusters". MNRAS, 505, 5978, 2021

[Vasiliev, 2019] - E. Vasiliev. "Proper motions and dynamics of the Milky Way globular cluster system from Gaia DR2". 2019.

[Wilkinson & Evans, 1999] - M.I. Wilkinson and N.W. Evans. "The present and future mass of the Milky Way halo". Monthly Notices of the Royal Astronomical Society, Volume 310, Issue 3, pp. 645-662, 1999.

[White & Frenk, 1991] - S.D.M. White and C.S. Frenk. "Galaxy Formation through Hierarchical Clustering". Astrophysical Journal v.379, p.52, 1991.

[Zavala & Frenk, 2019] - J. Zavala 1 and C.S. Frenk. "Dark Matter Haloes and Subhaloes". Galaxies 7, no. 4: 81, 2019.

[Zoccali et al. 2003] - M. Zoccali, A. Renzini, S. Ortolani, L. Greggio, I. Saviane, S. Cassisi, M. Rejkuba, B. Barbuy, R. M. Rich, and E. Bica. "Age and metallicity distribution of the Galactic bulge from extensive optical and near-IR stellar photometry". Astronomy and Astrophysics, v.399, p.931-956, 2003.

Acknowledgments

I would not be at this point in my life without my dear family and friends; their constant support over the last few years was fundamental in achieving one of the main goals of my life to date.

Thanks to the Ulisse Programme for giving me the opportunity to have an amazing experience of studying abroad and travelling to the other side of the world. I met many special people and had breathtaking moments that will forever remain in my heart.

In particular, my thanks go to Prof. Giovanni Carraro for the constant support, not only from an academic point of view but also as a human being; he pushed me towards the Ulisse Programme and it is because of him that I improved and became a better version of myself.

Another round of thanks goes to Prof. Vladimir Korchagin of Southern Federal University, as well as Roman Tkachenko, Anja Mailova and her father Boris, Nadia Klyuchko, Alexei Moiseev and his wife Aleksandrina Smirnova, Sergey Kotov and his wife Maria Kotova; all of them helped me to deal with everyday life in the Russian Federation as an Italian with absolutely no knowledge of the Russian language at all. I learnt so much from each of you, but most of all, I learnt to be kind to strangers in the most natural way.

Not to mention all the other students at Southern Federal University from all over the world. I belonged to an amazing international community that represents the most pure and natural human emotions: love for people, love to be a part of something, love for equity. I stand with them, foreigners in another country, and with the Ukrainian and Russian people who are trying to fight against a sick government that is slowly consuming their nations. This is also for you, my new sisters and brothers: Ali, Amoi, Bola, Hyunju, Jerry, Jiyhe, Jundi, Kevin, Mane, Nicole, Rina, and Steven.

At this point, even if these acknowledgements seem to be associated with the end of a journey, I think this will be just another beginning.

One should be proud of themselves and all the people with whom they have walked, and so I am: let us walk together towards new horizons, step by step, heart in hands.